KRASQ61H preferentially signals through MAPK in a RAF dimer-dependent manner in non-small cell lung cancer

$KRAS^{Q61H}$ preferentially signals through MAPK in a RAF dimer-dependent manner in non-small cell lung cancer

Zhi-Wei Zhou[1,†], Chiara Ambrogio[2,3†], Asim K Bera[1,†], Qing Li[4,†], Xing-Xiao Li[1], Lianbo Li[1], Jieun Son[2], Sudershan Gondi[1], Jiaqi Li[2], Emily Campbell[5], Hua Jin[6], Jeffrey J. Okoro[2], Cheng-Xiong Xu[4*], Pasi A. Janne[2,7*], Kenneth D. Westover[1*]

[1]Departments of Biochemistry and Radiation Oncology, The University of Texas Southwestern Medical Center at Dallas, Dallas, TX 75390, USA.

[2]Department of Medical Oncology, Dana-Farber Cancer Institute, Boston, MA 02215, USA.

[3]Department of Molecular Biotechnology and Health Science, Molecular Biotechnology Center, University of Torino, Torino, Italy

[4]Cancer Center, Daping Hospital and Research Institute of Surgery, Third Military Medical University, Chongqing 400042, China.

[5]Department of Physiology and Developmental Biology, Brigham Young University, Provo, UT 84604, USA

[6]Department of Thoracic Surgery, Daping Hospital and Research Institute of Surgery, Third Military Medical University, Chongqing 400042, China.

[7]Belfer Center for Applied Cancer Science, Dana-Farber Cancer Institute, Boston, MA 02215, USA.

Running title: $KRAS^{Q61H}$ signals in a RAF dimer-dependent manner

[†]These authors contributed equally.

*Correspondence to: Cheng-Xiong Xu, Cancer Center, Daping Hospital and Research Institute of Surgery, Third Military Medical University, 10 Changjiang Zhi Road, Yuzhong District, Chongqing 400042, China, Phone: +86 023 6875 7169; E-mail: xuchengxiong@hanmail.net; Pasi A. Janne, Dana-Farber Cancer Institute, 450 Brookline Avenue, LC4114, Boston, MA 02215. Phone: 617-632-6036; E-mail: pasi_janne@dfci.harvard.edu; Kenneth D. Westover, Departments of Biochemistry and Radiation Oncology, UT Southwestern Medical Center, 5323 Harry Hines Boulevard, Dallas, TX 75390. Phone: 214-645-0323; E-mail: kenneth.westover@utsouthwestern.edu.

Conflict of interest: P.A.J. has received consulting fees from AstraZeneca, Boehringer-Ingelheim, Pfizer, Roche/Genentech, Takeda Oncology, ACEA Biosciences, Eli Lilly and

Company, Araxes Pharma, Ignyta, Mirati Therapeutics, Novartis, LOXO Oncology, Daiichi Sankyo, Sanofi Oncology, Voronoi, SFJ Pharmaceuticals and Biocartis; receives post-marketing royalties from DFCI owned intellectual property on EGFR mutations licensed to Lab Corp; has sponsored research agreements with AstraZeneca, Daichi-Sankyo, PUMA, Boehringer Ingelheim, Eli Lilly and Company, Revolution Medicine and Astellas Pharmaceuticals; and has stock ownership in LOXO Oncology and Gatekeeper Pharmaceuticals. K.D.W has received consulting fees from Sanofi Oncology, is a member of the SAB for Vibliome Therapeutics and has or had sponsored research agreements with Astellas Pharmaceuticals and Revolution Medicine. K.D.W. declares that none of these relationships are directly or indirectly related to the content of this manuscript.

Materials & Correspondence: Crystal structure data is deposited in the PDB under code 6MNX. All other data is available in the main text or the supplementary materials. Requests for materials should be addressed to K.D.W. (kenneth.westover@utsouthwestern.edu) or (pasi_janne@dfci.harvard.edu) P.A.J.

Abstract

Assembly of RAS molecules into complexes at the cell membrane is critical for RAS signaling. We previously showed that oncogenic KRAS codon 61 mutations increase its affinity for RAF, raising the possibility that $KRAS^{Q61H}$, the most common KRAS mutation at codon 61, upregulates RAS signaling through mechanisms at the level of RAS assemblies. We show here that $KRAS^{Q61H}$ exhibits preferential binding to RAF relative to PI3K in cells, leading to enhanced MAPK signaling in *in vitro* models and human NSCLC tumors. X-ray crystallography of $KRAS^{Q61H}$:GTP revealed that a hyper-dynamic switch 2 allows for a more stable interaction with switch 1, suggesting that enhanced RAF activity arises from a combination of absent intrinsic GTP hydrolysis activity and increased affinity for RAF. Disruption of $KRAS^{Q61H}$ assemblies by the RAS oligomer-disrupting D154Q mutation impaired RAF dimerization and altered MAPK signaling but had little effect on PI3K signaling. However, $KRAS^{Q61H}$ oligomers but not $KRAS^{G12D}$ oligomers were disrupted by RAF mutations that disrupt RAF-RAF interactions. $KRAS^{Q61H}$ cells show enhanced sensitivity to RAF and MEK inhibitors individually whereas combined treatment elicited synergistic growth inhibition. Furthermore, $KRAS^{Q61H}$ tumors in mice exhibited high vulnerability to MEK inhibitor, consistent with cooperativity between $KRAS^{Q61H}$ and RAF oligomerization and dependence on MAPK signaling. These findings support the notion that $KRAS^{Q61H}$ and functionally similar mutations may serve as predictive biomarkers for targeted therapies against the MAPK pathway.

SIGNIFICANCE: Findings show that oncogenic $KRAS^{Q61H}$ forms a cooperative RAS-RAF ternary complex which renders RAS-driven tumors vulnerable to MEKi and RAFi, thus establishing a framework for evaluating RAS biomarker-driven targeted therapies.

Introduction

Activating *KRAS* mutations are major genetic drivers of aggressive cancers such as pancreatic ductal adenocarcinoma (PDAC), colorectal cancer (CRC), and lung adenocarcinoma (LUAD) (1). Development of RAS-directed therapeutic strategies has been challenging, but recent progress with $KRAS^{G12C}$ inhibitors (2-4) has ignited new hope for addressing *RAS*-driven diseases. However, the G12C story also suggests that other RAS mutations may require mutation-specific approaches derived from detailed understanding of mechanisms (5). Most oncogenic *RAS* mutations occur at codons 12, 13, and 61 (1). These mutations lead to accumulation of RAS-GTP, the activated form of RAS. However, the transforming potency of these mutations differ, and they occur at different rates across cancer types, suggesting that selection occurs in disease because of functional dissimilarities between mutations (1,5). Although we have no mechanistic explanations for why certain RAS mutations occur selectively in specific diseases, clues are beginning to emerge. For example, we recently showed that $KRAS^{A146T}$ and $KRAS^{V14I}$ activation occurs because of rapid nucleotide exchange (RNE) stemming from structural changes in the protein, instead of insensitivity to GTPase-activating proteins (GAPs) (6,7). This suggests that RNE mutants will occur selectively in contexts where RNE is supported, and/or where GAPs are deficient. On the other hand, the forces driving selection of other mutations, such as codon 13 and codon 61 mutations, are poorly understood.

Formation of RAS complexes at the cell membrane is essential for RAS signaling activity in many contexts (8-12). These complexes appear to be highly dynamic suggesting that specific RAS mutations may differentially alter the behavior of these sensitive complexes. Recently we reported a RAS mutation, D154Q, which neutralizes the suppressive effects of $KRAS^{WT}$ in the context of oncogenic KRAS. This mutation was designed based on a RAS-RAS interaction that

occurs via an α4-α5 interface seen in some RAS crystal structures (12). Recent NMR studies of RAS molecules bound to nanodisks also showed a similar structural model that utilizes the α4-α5 interface, although there were some differences (13). Nevertheless, the dynamic nature of these complexes suggests that multiple forms likely exist and other competing models have also been proposed, although they have not yet been evaluated in cell-based systems (14,15). Regardless, the ability to manipulate at least one form of RAS-RAS interaction using the D154Q mutation enables studies of how specific oncogenic RAS mutations may affect RAS assemblies.

RAS mutations that alter the strength of interactions with specific effectors have potential to alter the behavior of RAS complexes. One such mutation is $KRAS^{Q61H}$, which shows a combination of exceptionally low GTPase activity and a relatively high affinity for RAF (16). Here we directly compared $KRAS^{Q61H}$, a rare mutation in human disease overall (<1% of KRAS), but the most common codon 61 mutation for KRAS in human diseases, to $KRAS^{G12D}$, the most common cancer-associated *RAS* mutation overall. We used laboratory models and clinical samples derived from a large patient cohort to evaluate the importance KRAS multimerization on MAPK and PI3K activity. We also evaluated the structural basis of the preference of $KRAS^{Q61H}$ for MAPK signaling using x-ray crystallography. Our data suggest a unique interdependence between RAS and RAF multimerization for $KRAS^{Q61H}$, but not $KRAS^{G12D}$. This interdependence leads to increased signaling through the MAPK pathway, and sensitivity to RAF and MEK inhibitors, suggesting that certain codon 61 mutations in RAS may be useful as predictive biomarkers for RAS-directed therapies.

Materials and Methods

Plasmids

pcDNA3-CFP (Cat#13030), pcDNA3-YFP (Cat#13033), PIK3CA (Cat#16643), and pBABEpuro-c-RAF (Cat#51124) plasmids were purchased from Addgene. $KRAS^{WT}$ plasmid was sourced from DNA2.0 (Cat#95005). $KRAS^{WT}$, PIK3CA, and c-RAF full-length fragments were inserted into CFP or YFP-containing vectors to obtain CFP-$KRAS^{WT}$, YFP-$KRAS^{WT}$, CFP-PI3KCA, YFP-PI3KCA, YFP-c-RAF, c-RAF-CFP, and c-RAF-YFP constructs. $KRAS^{G12D}$, $KRAS^{G13D}$, $KRAS^{Q61H}$, $KRAS^{G12D/D154Q}$, $KRAS^{G13D/D154Q}$, $KRAS^{Q61H/D154Q}$, and $KRAS^{D154Q/R161E}$ mutants; and c-RAF^{R89L} and c-$RAF^{R89L/R401H}$ mutants were generated via site directed mutagenesis using *Pfu*UItra II Hotstart PCR Master Mix (Cat#600850-51). Constructs contain mCherry-H2B-P2A linked $KRAS^{G12D}$, $KRAS^{G13D}$, $KRAS^{Q61H}$ and the counterparts with D154Q mutation were generated using Gibson Assembly approach. For bacterial expression purpose, Raf-1-RBD^{1-149} plasmid (Cat#13338) was bought from Addgene, and p110γ-$RBD^{206-311}$ was constructed via Gibson Assembly using p110γ-$RBD^{206-311}$ fragment synthesized from IDT and Raf-1-RBD^{1-149} plasmid as a vector. The sequences were confirmed by DNA sequencing.

Cell Lines

HEK293T cells were purchased from the ATCC. *KRas*^{lox} $KRAS^{MUT}$ cells were generous gifts from Dr. Mariano Barbacid's lab and the generation has been previously described (17). All cells were obtained at the end of 2016. Briefly, $KRAS^{G12D}$ and $KRAS^{Q61H}$ retroviral plasmids were created by point mutagenesis from pBABE HA-tagged $KRAS^{WT}$ plasmid (provided by Channing Der, Addgene plasmid # 75282). Retroviruses were generated by co-transfection of pBABE plasmids together with pAmpho plasmid into HEK293T cells using FuGENE® HD

Transfection Reagent (Promega). The retroviruses were transduced into *HRas*$^{-/-}$; *NRas*$^{-/-}$; *KRas*$^{lox/lox}$ MEFs followed by 2 wks of puromycin selection (1 μg/mL) in DMEM medium supplemented with 10% fetal bovine serum (FBS), 100 g/ml penicillin and 100 units/ml streptomycin. To obtain *KRas*^{lox} KRAS^{MUT} clones, cells were then cultured in the presence of 4-hydroxytamoxifen (4OHT) (Sigma, H7904) for another 2 wks in order to achieve complete deletion of endogenous *KRas* alleles. Doxycycline (DOX) (Sigma, D9891) inducible Flp-In T-REx 293 cells expressing KRAS G12D, G13D, and Q61H and the counterparts with D154Q mutation were generated by following manufacturer's instructions (Thermal Fisher). In brief, constructs contain mCherry-H2B-P2A linked KRAS^{G12D}, KRAS^{G13D}, KRAS^{Q61H} and the counterparts with D154Q mutation were co-transfected with pOG44 into Flp-In T-REx 293 cells followed by 2 wks of hygromycin (100 μg/mL) and blasticidin (15 μg/mL) selection in DMEM medium supplemented with 10% Tet-free FBS (Omega Scientific, FB-15). DOX (2 ng) was added to induce protein expression and initiate RAS dimerization (8). All cell lines used in the study tested negative for Mycoplasma as determined by the Mycoplasma Plus PCR Primer Set (Agilent) and the most recent test was done in December 2019. The length of time between thawing and the use in the described experiments was always < 3 months.

Cellular Thermal Shift Assay

The protein thermal stability was evaluated via cellular thermal shift assay (CETSA) as previously described (18). HEK293T cells were co-transfected with KRAS mutants and c-RAF or p110α for 48 hrs. with the supplement of 10% FBS, then the protein samples were subject to thermal treatment using PCR machine. The resultant supernatants were then tested via Western blotting assay.

RAS-GTP Assay

HEK293T cells were grown in 10% FBS and RAS-GTP levels were assessed by Active Ras Pull-down Detection Kit (Thermal Fisher) using Raf-1-RBD and p110γ-RBD fused to GST to bind active (GTP-bound) RAS. Protein lysates (500 μg) were incubated with 100 μl glutathione resin and GST protein binding domains for 1 hr at 4ºC to capture active small GTPases according to the manufacturer's protocol. After washing, the bound GTPase was recovered by eluting the GST-fusion protein from the glutathione resin. The purified GTPase was detected by Western blotting assay using anti-RAS antibody.

Western Blot Analysis

Cells from *in vitro* culture, *ex vivo* explants, or NSCLC patient tumor specimens were lysed in RIPA lysis buffer (Thermo Fisher) supplemented with protease and phosphatase inhibitor cocktails (Sigma). The proteins of interest were probed with corresponding antibodies. Primary antibodies included anti-RAS (CST, 3339), anti-HA (CST, 2367), anti-HSP90 (Santa Cruz, sc-7947), anti-pAKT (Ser473, CST, 4060), anti-AKT (CST, 9272), anti-p-ERK1/2 (CST, 4370), anti-ERK (CST, 4695), anti-pMEK (CST, 9154), anti-MEK (CST, 8727), anti-pS6 (Ser235/236, CST, 4858), anti-S6 ribosomal protein (CST, 2217), anti-p-c-RAF (Ser259, 9421; Ser338, 9427), anti-c-RAF (CST, 53745), anti-c-RAF (Santa Cruz, sc-227), and anti-BIM (CST, 2933). Secondary antibodies included HRP-linked anti-rabbit IgG (CST, 7074) and anti-mouse IgG (CST, 7076).

Guanine Nucleotide Exchange Assays

KRAS proteins were preloaded with 2'/3'-O-(*N*-Methyl-anthraniloyl)-guanosine-5'-[(β,γ)-imido]triphosphate (Mant-GppNHp; Jena Biosciences) in 20 mM Tris pH 7.5, 50 mM NaCl, 200 mM $(NH_4)_2SO_4$ and 0.1 mM EDTA for 2 hrs at 25°C. The Mant-loaded KRAS proteins were exchanged into 20 mM Tris pH 7.5, 150 mM NaCl, 5 mM $MgCl_2$ and 5 mM EDTA using Zeba Spin Desalting Columns (Thermo Fisher Scientific). The Mant-loaded KRAS proteins were diluted 8 μM and incubated with p110γ-RBD at 25°C for 1 hr. Nucleotide dissociation was initiated by addition of 500-fold excess of unlabeled GTP, and the nucleotide dissociation rate was determined by the fluorescence emission at 448 nm (excitation 365 nm) using plate reader Synergy NEO (BioTek Instruments).

Human Specimens

Tumor specimens were obtained from 1,006 NSCLC patients during surgery at the Daping Hospital and Research Institute of Surgery, Third Military Medical University, Chongqing, China. Western blotting and immunohistochemistry assays were performed as previously described (19). The assessment of the staining was scored independently by two pathologists without knowledge of the clinicopathological findings. Mutation of *KRAS*, *EGFR*, *PI3K*, *ALK*, and *BRAF* was detected using SurPlex™ liquid chip at SurExam Bio-Tech Co. Ltd (Guangzhou, China). This research was approved by the Research Ethics Board of the Daping Hospital and Research Institute of Surgery.

Histopathology and Immunohistochemistry

Tumor tissues from NSCLC patients were fixed in 10% buffered formalin (Sigma), embedded in paraffin, and sectioned at 4 μm. The tissue sections were stained with Haematoxylin & Eosin (H&E), and performed histopathological analysis. Immunohistochemistry was performed as described previously (19), and the IHC staining intensity was scored as 0, 1, 2, and 3 (0, none; 1, weak staining; 2, moderate staining; and 3 strong staining). All pathologic analysis and IHC scoring were performed by two independent pathologists. To evaluate for the percentage of p-AKT or p-ERK staining positive cells, five fields were randomly selected per section (at ×40), and counted the total and staining positive cells for each field, then calculated the average percentage of cells stained positively. H-score was applied to evaluate for p-AKT and p-ERK according to the following formula: H-score = weak intensity (1) × percentage + moderate intensity (2) × percentage + strong intensity (3) × percentage. The following antibodies were used for immunostaining: p-ERK (CST, 9101) and p-AKT (CST, 4060).

Protein Expression and Purification

A construct encoding codon-optimized N-terminal His-tobacco etch virus (TEV)-$KRAS^{Q61H}$ in the pJExpress vector (DNA2.0) was synthesized and used to transform BL21 (DE3) cells. Cells were grown in Luria broth (LB) to OD600 0.9 and induced with 0.5 M isopropyl β-D-1-thiogalactopyranoside (IPTG) for 16 hrs at 16 °C. Cells were pelleted and re-suspended in lysis buffer [20 mM sodium phosphate (pH 8.0), 500 mM NaCl, 10 mM imidazole, 1 mM 2-mercaptoethanol (BME), 5% (vol/vol) glycerol] containing 1 mg/mL PMSF and benzamidine as protease inhibitor. Lysates were flash-frozen and stored at −80 °C until use. Protein was purified over an IMAC cartridge (BioRad) following standard Ni-affinity protocols

and desalted into 20 mM HEPES (pH 8.0), 150 mM NaCl, 5 mM $MgCl_2$, and 0.5 mM DTT buffer. The N-terminal His tag was cleaved by 24 hrs digestion with a 1:10 ratio of TEV protease at 4 °C, and the TEV with His-tag were removed by reverse purification over an IMAC cartridge. Protein was concentrated to 30 mg/mL in a 10-kDa cutoff Amicon filter (Millipore), aliquoted, and then flash-frozen and stored under liquid nitrogen until use. Yields were ~8 mg of purified Q61H mutant of KRAS per liter of culture.

Raf-1-RBD$^{1-149}$ and p110γ-RBD$^{206-311}$ were expressed in BL21 (DE3) *E. coli*. Cells were induced by 1 mM IPTG (A_{600} between 0.6 and 0.8) for 3 hrs at 37^{o}C, then homogenized in PBS containing 1 mM EDTA, 1% Triton X-100, and 1% protease inhibitor. The lysate was centrifuged and resultant supernatant was purified over a GST column. Purified RBDs were flash-frozen and stored at −80 °C until use. Yields were ~10 mg of purified Raf-1-RBD and ~4 mg of purified p110γ-RBD per liter of culture.

Crystallization and Structure Solution

GDP-loaded KRAS Q61H variant were concentrated to 30 mg/ml. Initial crystallization trials were performed with a Mosquito (TTPLabTech) crystallization robot using the sitting-drop method (100 nl protein plus 100 nl crystallization solution). Right before crystallization set up 20 mM GTP supplemented in protein. Initial hit at 20 °C with 0.1M MMT and 24% PEG 6000 observed. The Crystal size and quality were improved using hanging/sitting-drop crystallization trials. Diffraction data were collected at SBC beamline 19-ID, Advanced Photon Source at the Argonne National Laboratory and processed using HKL3000 (20). Crystal belongs to primitive orthorhombic symmetry and diffracted to 2.19 Å. The structure of Q61H was solved by

molecular replacement using PHASER in CCP4 suite (21), with the structure of $KRAS^{WT}$ (PDB ID: 4OBE) used as search model. There are six $KRAS^{Q61H}$ molecules in the asymmetric unit (solvent content 47.5%). After PHASER we could see clear density of GTP at nucleotide binding site in each of the six models. Coot (22) was used for model building and PHENIX (23) was used for refinement at 2.19 Å resolution. The final atomic model contains six GTP for each of the six copies of the GTP-Q61H complex and structure quality monitored by MolProbity (24). RMSDs are calculated by lsqkab script in CCP4 suite for structure comparisons and PyMOL (The PyMOL Molecular Graphics System, Version 1.5.0.4 Schrödinger, LLC) was used for structural figures.

Molecular Dynamics (MD) Simulations

The Schrödinger package on the Maestro platform (Schrödinger release 2016-2, Maestro, version 10.6, Schrödinger, LLC) was used to perform molecular dynamics. Systems were prepared from high-resolution crystal structures of $KRAS^{G12D}$ mutant bound with GNP (PDB ID: 5USJ) which was prepared for model construction using the Protein Preparation module, including missing atoms addition, H-bond assignment, and restrained minimization. All simulation systems were neutralized via adding charge-neutralizing counter ions in a 10 Å buffering distance in the SPC solvent model. No ion-excluded region was included. The 50 ns simulations were performed using the Desmond Molecular Dynamics module with a constant temperature (300 K) and pressure (1.0 bar) in the NPT ensemble.

FRET assay

The FRET assay was performed as previously described (12). Briefly, HEK293T cells were co-transfected with the paired CFP- and YFP-fused KRAS constructs and c-RAF constructs under the condition of 10% FBS in 2-well chambered coverglass (Lab-Tek™). After 36-48 hrs, live cell imaging was performed using a Confocal/Multiphoton Zeiss LSM880 microscope. Data were collected from three biological repeats and 10–12 different cells in different fields from the same coverslip selected for microscopy. Quantitation was done using ZEN software (ZEISS).

Calculation of D154Q dependency ratio

Western blots were quantitated as described above. Ratios of pERK for WT vs D154Q-containing specimens were calculated as follows.

$$D154Q\ dependency\ ratio_{MAPK} = \frac{pERK_{KRAS\ WT}}{pERK_{KRAS\ D154Q}}$$

$$D154Q\ dependency\ ratio_{PI3K} = \frac{pAKT_{KRAS\ WT}}{pAKT_{KRAS\ D154Q}}$$

Where pERK is the ratio of pERK to tERK.

Growth Assessment by IncuCyte

KRas^{lox} KRAS^{MUT} Cells (1×10^3) were seeded in 96-well plates in 150 µL DMEM complete medium. The following day, plates were treated with selumetinib (Selleck Chem, 100 nM), trametinib (Selleck Chem, 10 nM), or RAF709 (Selleck Chem, 1 µM) alone or in combination and incubated in the IncuCyte Zoom for real-time imaging, with three fields imaged per well under 10x magnification every 2 hrs. Data were analyzed using the IncuCyte

Confluence version 1.5 software, which quantified cell surface area coverage as confluence values. IncuCyte experiments were performed in triplicate. A single representative growth curve is shown for each condition.

To assess the effects of D154Q on cell growth, DOX inducible Flp-In T-REx 293 cells (1×10^3) expressing KRAS G12D, G13D, and Q61H and the counterparts with D154Q mutation were seeded in black 96-well plates with clear bottom in 200 μL DMEM complete medium with supplement of DOX (2 ng) and incubated in the IncuCyte Zoom for real-time imaging, with three fields imaged per well under 10x magnification every 4 hrs. Data were analyzed using the IncuCyte software, which counted red cell nucleus (mCherry-H2B location) as cell number. IncuCyte experiments were performed in triplicate.

Drug Sensitivity Assay

MEK and RAF inhibitors sensitivity was tested in $KRAS^{G12D}$ and $KRAS^{Q61H}$ expressing *Ras*less MEF cells when treated alone or in combination. Cells (1×10^3) were seeded in 96-well plates in DMEM complete medium. The following day, cells were treated with selumetinib, trametinib, or RAF709 alone using a ten-point dose titration scheme from 1 nM to 10 μM, from 1 nM to 1 μM, from 1 nM to 10 μM, respectively. In addition, cells received a combinatorial treatment with selumetinib or trametinib at various concentrations and a fixed concentration of RAF709 at 1 μM; or with RAF709 at various concentrations and a fixed concentration of selumetinib and trametinib at 1 μM and 10 nM, respectively. After 72 hrs, cell viability was assessed using colorimetric MTS assay (CellTiter 96® AQueous Non-Radioactive Cell Proliferation Assay (MTS) Powder, Promega). Absolute inhibitory concentration (IC) values were calculated using four-parameter logistic curve fitting. All experimental points were a result

of three to six replicates, and all experiments were repeated at least three times. The data was graphically displayed using GraphPad Prism 5 for Windows (GraphPad Software). Each point (mean ± standard deviation) represents growth of treated cells compared to untreated cells. The curves were fitted using a non-linear regression model with a sigmoidal dose response.

Drug Synergy Analysis

Cells were plated at a concentration of 1,000 cells/well in a 384 well plate and allowed to settle for 24 hrs. The cells were then treated with a serial dilution of drugs in a 7×7 format with up to 6 repeats per plate using an HP D300e Digital Dispenser. After an additional 72 hrs, CellTiter-Glo reagent was added to each well and the luminescence readout was evaluated by a POLARStar Omega Plate Reader. The relative viability was then calculated by dividing the reading of each well by the reading from the untreated control. The program Combenefit (25) was then used to calculate a Bliss Synergy Score for each drug combination and generate graphs, with higher scores indicating greater synergy. The number of asterisks below the synergy score indicate statistical significance as follows: * $P<0.05$, ** $P<0.001$, *** $P<0.0001$.

Animal Models

Crl:NU-*Foxn1*^{nu} mice (females, 6 to 8-week-old) were purchased from Charles River. *KRas*^{lox} KRAS^{MUT} cells (1×10^6) were injected subcutaneously in a 1:1 mix of serum-free DMEM and Matrigel (phenol red–free; BD Biosciences) in both flanks of recipient mice. Once a palpable tumor formed, measurements were taken daily using calipers. Drug-naïve mice bearing established tumors of 240 to 300 mm^3 were randomly assigned to either selumetinib or vehicle treatment. Selumetinib, solubilized in 1% carboxymethyl cellulose (CMC), 0.25% Tween 80 was

administered daily by oral gavage (0.1 mL/10 g body weight) at a dose of 50 mg/kg in drug-naïve mice. Animals randomly assigned to experimental treatment groups were dosed by oral gavage without blinding at any stage of the study. Welfare-related assessments and interventions were carried our daily during the treatment period. All care and treatment of experimental animals were in strict accordance with Good Animal Practice as defined by the US Office of Laboratory Animal Welfare and approved by the Dana-Farber Cancer Institute Institutional Animal Care and Use Committee.

Statistical and Data Analysis

Unless otherwise specified, data are presented as mean ± SD. Significance between two groups was assessed by the Student's two-tailed t-test. Data sets consisting of more than 2 groups were analyzed by analysis of variance (ANOVA). A p value that was less than 0.05 was considered statistically significant for all data sets. All statistical analysis was performed using GraphPad Prism software. No statistical method was used to predetermine sample size in animal studies. The investigators were blinded during evaluation of tumor size variations following treatments.

Results

$KRAS^{Q61H}$ Preferentially Binds to c-RAF

We previously evaluated the relative binding affinities of a panel of activating RAS mutants for RAF in a purified system and found a range of values (16). We speculated that this could lead to preferential signaling events, but considered that comparisons to interactions with other canonical RAS effectors may provide additional insights. We applied three different approaches

to determine if $KRAS^{Q61H}$ preferentially interacts with c-RAF as compared to the catalytic subunit of type I PI3K, also known as p110α and p110γ, which regulates cell cycle, survival, metabolism, and other processes (26) (Fig. 1A). As a control, we included $KRAS^{G12D}$, which has been demonstrated to signal through both PI3K and MAPK pathways (27), and $KRAS^{G13D}$ which shows intermediate binding affinity toward RAF (16). We first used c-RAF-RBD or p110γ-RBD to pull down mutant KRAS expressed in HEK293T cells in the presence of 10% FBS to stimulate RAS signaling. $KRAS^{Q61H}$ recovery by RAF-RBD was enhanced as compared to $KRAS^{G12D}$, whereas $KRAS^{G12D}$ showed a minor, though statistically significant, enhancement in binding to p110γ-RBD compared to $KRAS^{Q61H}$ (Fig. 1B and 1C), suggesting $KRAS^{Q61H}$ preferentially binds to c-RAF-RBD.

To evaluate if these preferential protein-protein interactions also occur in cells, we used CETSA that evaluates protein stability *in situ* (18). In this technique, proteins that are resistant to thermal treatment are interpreted to be stabilized by other factors, in this case partnering proteins. We compared $KRAS^{G12D}$, $KRAS^{WT}$, and $KRAS^{Q61H}$ for the ability to interact with c-RAF or p110α. c-RAF was more stable in the presence of $KRAS^{Q61H}$ when compared to $KRAS^{WT}$, or $KRAS^{G12D}$, although $KRAS^{G12D}$ also enhanced c-RAF thermal stability to some degree over $KRAS^{WT}$ (Fig. 1D). On the other hand, p110α was more resistant to thermal exposure in the presence of $KRAS^{G12D}$ and, to a lesser degree, $KRAS^{Q61H}$, in comparison to $KRAS^{WT}$ (Fig. 1E). We also tested KRAS thermal stability, but saw no statistical difference between KRAS mutant samples irrespective of c-RAF or p110α expression (Supplementary Fig. S1A and S1B).

As another strategy, we tested the nucleotide dissociation rate for $KRAS^{G12D}$ and $KRAS^{Q61H}$ in the presence of p110γ-RBD. Productive binding between RAS and p110γ-RBD would be predicted to slow the dissociation of nucleotide from RAS. We observed this for $KRAS^{G12D}$ but

saw no stabilizing effect for $KRAS^{Q61H}$, suggesting a lack of interaction between $KRAS^{Q61H}$ and p110γ-RBD within the bounds of this assay (Supplementary Fig. S1C and S1D). Taken together, these results suggest that $KRAS^{Q61H}$ preferentially binds to c-RAF over p110α/γ relative to $KRAS^{G12D}$.

$KRAS^{Q61H}$ NSCLC Preferentially Signals through MAPK

The asymmetric physical interactions between $KRAS^{Q61H}$ or $KRAS^{G12D}$ and c-RAF or p110γ predict that corresponding effects will propagate to intracellular signaling. We hypothesized that $KRAS^{Q61H}$ mutations in patients would also show a preferential signaling pattern through MAPK over PI3K/AKT. To explore this, we examined MAPK and PI3K/AKT signaling activity in NSCLC patient specimens. We screened 1,006 NSCLC patient frozen specimens for mutations in *KRAS, EGFR, PI3K, ALK,* or *BRAF* and identified 59 cases with *KRAS* mutations (Fig. 2A), which is consistent with reported mutation frequency in Asian with high *EGFR* (30%-40%) and low *RAS* (3%-8%) mutation (28,29). Of these, three contained $KRAS^{Q61H}$ mutations. A summary of the study population is given in Table S1. We randomly selected additional samples with $KRAS^{WT}$ or $KRAS^{G12D}$ mutations for comparison. By IHC analysis, both oncogenic *KRAS* mutations showed higher levels of p-AKT and p-ERK as compared to wild-type KRAS. However, $KRAS^{G12D}$-driven NSCLC showed more prominent p-AKT staining compared to $KRAS^{Q61H}$-containing NSCLC (Fig. 2B and C). To further quantify these differences, Western blots of tumor tissues showed a significantly higher level of p-ERK signaling in $KRAS^{Q61H}$ samples as compared to $KRAS^{G12D}$ samples, while p-AKT levels were significantly higher in $KRAS^{G12D}$ compared to $KRAS^{Q61H}$ specimens (Fig. 2D and E; Supplementary Fig. S2A and S2B). The RAS level was not significantly different in $KRAS^{G12D}$

and *KRAS*^{Q61H} specimens (Fig. 2D and E, Supplementary Fig. S2A and S2B). These data suggest that the preferential signal output of KRAS^{Q61H} through MAPK signaling pathway also occurs in NSCLC clinical specimens.

A Hyper-dynamic Switch 2 Explains Preferential MAPK Signaling

The selective preferential interactions of KRAS^{Q61H} for MAPK argues that the Q61H mutation causes structural changes in KRAS^{Q61H} that are not seen in KRAS^{G12D}. We solved an X-ray crystal structure of KRAS^{Q61H} lacking a hypervariable C-terminal domain (residues 1-169) in complex with GTP (Supplementary Table S2; Fig. 3A-F). The fact that we were able to use GTP instead of a non-hydrolysable analogue is a remarkable re-demonstration of the negligible GTPase activity of this mutant (16) because protein crystallization takes 2-3 days. Crystals were in the $P2_12_12_1$ space group such that six molecules were in the asymmetric unit. Unambiguous electron density was observed for all molecules except for two residues in molecule A and three residues in molecule F (missing residues: Chain A 64 and 65; Chain F 62-64). Density was also observed for GTP, a magnesium ion, and water molecules (Fig. 3B). The conformation resembles previously reported GTP analogue-bound RAS structures with the exception of the rearrangement of switch 2, which, when all 6 molecules from the asymmetric unit are superimposed and compared, presents an ensemble of backbone and residue 61 sidechain conformations (RMSD 4.6 Å) within the crystal lattice (Fig. 3G). This is dissimilar to prior GTP-analogue bound RAS structures including KRAS^{Q61H}-GMPPNP (PDB ID: 3GFT), HRAS^{G12D}-GMPPNP (PDB ID: 1AGP), KRAS^{G12D}-GMPPNP (PDB ID: 5USJ), and HRAS^{G12C}-GMPPNP (PDB ID: 4L9W) where the position of codon 61 sidechains generally align (RMSD 0.8 Å), approximately 6 Å from the γ phosphate (Fig. 3H). The average B-factors of switch 2 residues

are around 2-fold higher than the rest of the structures, reflecting their dynamic character. On the other hand, switch 1 is well-ordered and resembles the previously described 'state 2' of GTP-bound RAS (30).

Given the array of side chain positions in residue 61, we inferred that altered interactions upon mutation of Gln to His drive the conformational dynamics of switch 2. To further demonstrate this effect, we performed MD simulations extending over 50 ns using a high-resolution X-ray structure of $KRAS^{G12D}$-GNP (PDB ID: 5USJ) as the seed model. In simulations pertaining to $KRAS^{Q61H}$, the side chain of residue 61 was computationally mutated to His without additional alterations. We examined the distances between the side chain nitrogen of residue 61 (Q or H) and γ phosphate of GTP over the course of the simulation (Fig. 3I**)**. Compared to Q61, H61 rapidly moves away from the gamma phosphate early in the simulation and tends to remain separated (Fig. 3J). To rationalize this effect, we considered that in other GTP-bound RAS structures, with the exception of other Q61 mutants, Q61 typically engages in a hydrogen bond network involving multiple side chains, water molecules, and the phosphate oxygens (Supplementary Fig. S3A and S3B). This includes contributions from Gln61, Glu62, Tyr64, Ala68, and Tyr96 which, in concert, hold switch 2 in a 'closed' conformation, bringing most of these side chains into close proximity with the gamma phosphate as seen in the structure of $KRAS^{G12D}$-GMPPNP (PDB ID: 5USJ) (Supplementary Fig. S3B). Of note, bridging waters, which normally play a role in catalysis, are key components of these interactions (31). With the mutation of Gln to His at position 61, the side chain no longer interacts with a key bridging water, leading to a breakdown in the remaining network and an unconstrained switch 2 (Fig. 3G-I). An unconstrained, hyper-dynamic switch 2 that does not interact significantly with the adjacent switch 1, is expected enable a more stable conformation of switch 1. This is because

switch 2 has the ability to induce more dynamic behavior in switch 1 under normal circumstances (32,33). A more stable conformation of switch 1 has the potential to lead to improved interactions with RAF, since switch 1 serves as the primary interface for RAS-RAF interactions (34).

Modeling our structure into prior structures of RAS in complex with effector proteins provides an additional possible reason why a dynamic switch 2 could lead to differential RAS-effector interactions. We superimposed our model of $KRAS^{Q61H}$-GTP onto that of $HRAS^{G12V}$-GNPPNP-p110γ (PDB ID: 1HE8) and HRAS-GNPPNP-RAF-RBD (4G0N). We noted that increased switch 2 flexibility has the potential to clash with p110γ, especially Tyr64 of $KRAS^{Q61H}$ and Phe221 of p110γ which are in close contact **(**Supplementary Fig. S4A and S4B**)**. However, with RAF-RBD, we note that increased switch 2 flexibility has the potential to enhance interactions between switch 1 and the RBD (Supplementary Fig. S4C) (33). Collectively, these observations suggest two possible structural mechanisms by which $KRAS^{Q61H}$ could favor binding to RAF-RBD over p110α/γ-RBD.

$KRAS^{Q61H}$ oligomerization and c-RAF dimerization are Interdependent

Interactions between RAS and p110α/γ or c-RAF might also be influenced by RAS-RAS interactions, which was previously shown to be important for RAS^{WT}-dependent suppression of cell growth (12). Interdependence of RAS-RAS and RAF-RAF interactions also seemed possible given that both are known to form complexes, and interactions between c-RAF and RAS are required to overcome the autoinhibitory function of the c-RAF N-terminal regulatory (NTR) region, allowing c-RAF to dimerize at the cell membrane (35). Additionally, ‘cooperativity’ between RAS and RAF is a component of proposed mechanisms of paradoxical MAPK signaling

in the presence of RAF inhibitors (36,37). Of note, we did not expect to see such cooperativity with PI3K, because PI3K multimerization is not known to occur. Moreover, extrapolation based on the structure of HRAS-p110γ (38), to include p110γ in our RAS dimer model predicts against any interaction between individual p110 protomers bound to dimerized RAS (Supplementary Fig. S5). Given the increased affinity of $KRAS^{Q61H}$ for RAF, and the lack of GTPase activity in $KRAS^{Q61H}$ which would be expected to allow for stable complex formation, we hypothesized that $KRAS^{Q61H}$, in particular, may show dependence on the formation of RAF dimers. Prior work showed that the D154Q substitution in KRAS was sufficient to disrupt KRAS-KRAS interactions at the cell membrane that occur via the KRAS α4-α5 interface, but did not alter the baseline biochemical properties of KRAS such as GTPase activity or affinity for RAF (39). The D154Q mutation also abolished the suppressive effects of $KRAS^{WT}$ seen in the genetic background of oncogenic KRAS. This was shown in the *Ras*less MEF model *in vitro* and *in vivo*, and in multiple cancer cell lines. Our interpretation was that the suppressive effects of $KRAS^{WT}$ occur through direct RAS-RAS interactions (12). Here we used the same mutation to study the impact of D154Q in the context of RAS^{Q61H}. Surprisingly, addition of D154Q impaired capture of $KRAS^{Q61H}$ by c-RAF, but did not alter $KRAS^{WT}$, $KRAS^{G12D}$, or $KRAS^{G13D}$ recovery. On the other hand, D154Q did not impact recovery by p110γ (Fig. 4A-C). Together these results suggest that KRAS multimerization influences interactions with c-RAF for $KRAS^{Q61H}$ but not p110γ in this cellular context.

To further evaluate interdependence between RAS and RAF interactions, we used a cell-based FRET assay to examine the influence of c-RAF interactions on KRAS and c-RAF multimerization (12). In the RAS assay, a CFP donor and an YFP acceptor are fused to the N-terminus of KRAS (Supplementary Fig. S6A-F). If CFP and YFP are adjacent, CFP is excited

and energy is transferred to YFP. However, CFP emission increases upon photobleaching due to loss of energy absorption by YFP. If CFP and YFP are spatially separated, no change in CFP emission is observed due to the absence of energy transfer from CFP to YFP (please see Fig S3B of (12) for a schematic of the assay principle). $KRAS^{WT}$ and $KRAS^{G12D}$ showed FRET in the presence of $c\text{-}RAF^{WT}$ that was minimally attenuated by the introduction of R89L into c-RAF, a mutation known to disrupt the RAF-RAS interaction for WT or $KRAS^{G12D}$ (40) (Fig. 4D; Supplementary Fig. S6A and S7A). However, $KRAS^{Q61H}$ multimerization was not detectable with introduction of R89L suggesting that $KRAS^{Q61H}$ depends on c-RAF for multimerization (Fig. 4D).

We noted that a RAS-RAS interaction can be also be detected without the introduction of exogenous c-RAF in the presence of 10% FBS (Supplementary Fig. S6B and S6C), suggesting that endogenous c-RAF is sufficient to influence RAS multimerization. We posited that exogenous $c\text{-}RAF^{R89L}$ acts indirectly upon RAS multimerization by sequestering endogenous RAF by RAF multimerization, leading to loss of FRET signal (Fig. 4E). To confirm this we introduced a second mutation R401H, which is known to disrupt RAF-RAF multimerization, to release any sequestration of endogenous RAF (41). Consistent with the hypothesis, exogenous $c\text{-}RAF^{R89L/R401H}$ restored $KRAS^{Q61H}$ multimerization (Fig. 4F; Supplementary Fig. S6D and S7A). Of note, MAPK signaling in the cell samples used for FRET was concordant with FRET results (Supplementary Fig. S7B). Specifically, overexpression of exogenous $c\text{-}RAF^{R89L}$ reduced c-RAF and ERK phosphorylation and for all forms of KRAS. However, the effect was more prominent in the context of $KRAS^{Q61H}$ (Supplementary Fig. S7B) suggesting that $KRAS^{Q61H}$ is regulated by RAF multimerization. Also similar to the FRET result, introduction of the combination of R401H and R89L mutations into c-RAF recovered p-ERK for $KRAS^{Q61H}$ but not $KRAS^{G12D}$

(Supplementary Fig. S7B), suggesting that release of sequestered endogenous RAF leads to restoration of an interdependent c-RAF- $KRAS^{Q61H}$ complex, but the same interdependence with c-RAF does not apply to $KRAS^{G12D}$. In aggregate, these results support that c-RAF multimerization is critical for regulation at the level of $KRAS^{Q61H}$ regulation, but to a lesser degree for $KRAS^{G12D}$.

The availability of this system also allowed us to examine if KRAS multimerization may similarly impact c-RAF multimerization. This question arises from work showing that certain RAF mutations are RAS-dependent for RAF multimerization (42). We measured the dependence of RAF multimerization on RAS multimerization using a c-RAF FRET assay similar in principle to the RAS multimerization assay. This assay is also similar in concept to previously reported BRET assays used to measure RAF interactions (43). In this assay c-RAF multimerization required overexpression of exogenous KRAS, but was lost upon introduction of D154Q demonstrating that c-RAF multimerization was dependent on RAS multimerization (Fig. 4G; Supplementary Fig. S6E and S6F). Taken together, these results demonstrate that $KRAS^{Q61H}$ and c-RAF multimerization events are interdependent.

$KRAS^{Q61H}$-mediated MAPK Signaling Is RAS multimer-dependent

To understand if the interdependence of RAF and KRAS dimers translates into biological differences in cell signaling, we examined $KRAS^{Q61H}$ and $KRAS^{G12D}$-dependent signaling in HEK293T cells expressing exogenous mutant KRAS proteins, focusing on p-ERK and p-AKT as indicators. Consistent with binding studies and patient tissue analysis (Fig. 1B and C; Fig. 2D and E), $KRAS^{Q61H}$ demonstrated enhanced activation of ERK relative to AKT, while $KRAS^{G12D}$ showed activation of both ERK and AKT (Fig. 4H). Addition of the D154Q mutation

significantly reduced p-ERK levels, while p-AKT levels were less affected. To better appreciate the impact of RAS mutations on multimerization for the MAPK vs. PI3K pathways, we quantitated a "D154Q dependency ratio" that consists of the ratio of p-ERK or p-AKT in the presence of WT vs. D154Q mutated KRAS as defined in the methods section. $KRAS^{Q61H}$-associated MAPK signaling was highly sensitive to D154Q compared to $KRAS^{G13D}$ and $KRAS^{G12D}$ **(**Fig. 4I). Additionally, for G13D and Q61H, MAPK signaling was sensitive to D154Q, whereas PI3K signaling was not. These results were reflected in the growth of these cells such that introduction of the D154Q into the exogenously-expressed KRAS also impaired cell growth (Fig. S8). Collectively, these results support that preferential interactions between $KRAS^{Q61H}$ and c-RAF rely on RAS multimerization to produce disproportionate up regulation of MAPK pathway signaling relative to PI3K/AKT.

$KRAS^{Q61H}$ Is a Marker of Sensitivity to MEK Inhibitors and an Allosteric RAF Inhibitor in vitro and in vivo

The observations that *$KRAS^{Q61H}$* preferentially signals through MAPK and depends on RAF multimerization raises the possibility that *$KRAS^{Q61H}$* bearing cells will be sensitive to inhibitors of these mechanisms. In particular we anticipated that RAF inhibitors that function in the context of the RAF dimer, such as RAF709 (44), would show increased activity in *$KRAS^{Q61H}$*. We exposed isogenic RAS-dependent MEF cells (12) to MEK inhibitors selumetinib and trametinib and RAF709. This system is derived from *Ras*-less mouse embryonic fibroblasts (MEFs) (17), in which the endogenous *HRas* and *NRas* alleles are constitutively knocked out and conditional *KRas* alleles are under the control of a resident 4OHT-inducible CRE recombinase, so that cells are dependent on introduction of an exogenous *Ras* gene for growth. For these

experiments we used MEFs with human HA-tagged *KRAS*^{G12D} and *KRAS*^{Q61H} (herein referred to *KRas*^{lox}KRAS^{MUT}). *KRas*^{lox}KRAS^{Q61H} MEFs were more sensitive to selumetinib and trametinib treatment than the *KRas*^{lox}KRAS^{G12D} MEFs for cell growth and proliferation. IC_{50} values for both selumetinib and trametinib were roughly 5-fold lower for Q61H as compared to G12D (Fig. 5A and B). However, we noted ~15-fold difference upon exposure to RAF709 (Fig. 5C) in favor of Q61H. A similar effect was also seen for both overall proliferation and growth kinetics (Fig. 5D). Co-treatment with RAF709 significantly decreased IC_{50} to selumetinib and trametinib in both *KRas*^{lox}KRAS^{G12D} and *KRas*^{lox}KRAS^{Q61H} MEFs, whereas either selumetinib or trametinib co-treatment further increased IC_{50} to RAF709 (Supplementary Fig. S9). Correspondingly, selumetinib, trametinib, and RAF709 showed stronger suppressive effects on MAPK signaling in *KRas*^{lox} KRAS^{Q61H} MEFs in comparison to *KRas*^{lox} KRAS^{G12D} MEFs as single agents (Supplementary Fig. S10A). We also evaluated for induction of the Bcl-2 family member BIM given that RAF/MEK/ERK signaling leads to inhibition of BIM (45). Consistent with this hypothesis, our *KRas*^{lox}KRAS^{MUT} system showed that BIM was dramatically upregulated in *KRas*^{lox} KRAS^{Q61H} cells rather than in *KRas*^{lox} KRAS^{G12D} cells when exposed to selumetinib, trametinib, or RAF709 alone (Supplementary Fig. S10A).

These differences persisted *in vivo* for a xenograft mouse model implanted with *KRas*^{lox} KRAS^{G12D} cells or *KRas*^{lox} KRAS^{Q61H} cells treated with selumetinib. Remarkably, tumors shrank in the Q61H group in response to selumetinib, while the G12D showed continued slow growth without evidence of actual tumor regression (Fig. 5G and Supplementary Fig. S10D).

Finally, we also noted that both *KRas*^{lox}KRAS^{G12D} and *KRas*^{lox}KRAS^{Q61H} showed enhanced sensitivity to combination treatment with MEK inhibitor and RAF709 (Fig. 5D; Supplementary Fig. S9; Supplementary Fig. S10B and S10C). We therefore evaluated for

synergy between RAF and MEK inhibition and found synergistic effects in both systems, as measured using the Bliss independence dose–response surface model (25,46). Bliss scores more than zero indicate combinations where the effect is greater than additive. Of note, synergistic effects between MEK inhibitors and RAF709 occurred at lower concentrations for $KRAS^{Q61H}$, relative to $KRAS^{G12D}$ (Fig. 5E and F; Supplementary Fig. S11A and S11B). Moreover, the combination resulted in a greater increase in BIM induction in $KRas^{lox}KRAS^{Q61H}$ MEFs (Supplementary Fig. S10A).

Discussion

Here we established that $KRAS^{Q61H}$ has a negligible intrinsic GTPase activity and a preferential interaction with RAF proteins over PI3K. In essence, the combination of the negligible GTPase activity and enhanced interaction with RAF appears to partially sequester $KRAS^{Q61H}$ into signaling though the MAPK pathway. The structural mechanism arises from disengagement of the switch 2 of RAS from the gamma phosphate of GTP, which both ablates GTPase activity and enhances interactions with RAF, but decreases interactions with p110γ. The enhancement of RAS-RAF interactions in turns leads to an interdependence of RAS and RAF multimerization. One result of this interdependence appears to be that *KRAS* mutant tumors bearing $KRAS^{Q61H}$ are more sensitive to inhibition of MAPK signaling at the level of RAF and MEK.

These observations may explain the rarity of $KRAS^{Q61H}$ mutations overall, either because it lacks sufficient interactions with PI3K which are essential for supporting RAS-driven tumorigenesis in certain contexts (47), or because unrestrained MAPK signaling leads to deleterious effects (48) in the absence of other, as yet unknown, compensatory factors. These

results also provide motivation for clinical trials exploring MAPK pathway inhibitors in mutational subsets of RAS-driven cancers. Specifically, these findings suggest that cancerous tumors bearing *KRAS* codon 61 mutations will be more sensitive to the inhibition of MAPK signaling pathway via MEK or 'paradox-breaking' RAF inhibitors as compared to codon 12 and 13 *KRAS* mutations.

Our findings also expand the understanding of the context-dependence of RAS multimerization/clusterization with respect to RAS mutations and effector interactions. Specifically we establish that an interdependence between RAS and RAF multimerization plays a special role with $KRAS^{Q61H}$, not seen with $KRAS^{G12D}$. Additionally, the D154Q substitution did not affect PI3K activity for either mutant, suggesting that RAS multimerization plays a role in MAPK, but not PI3K signaling. This property raised the hypothesis that $KRAS^{Q61H}$ would show enhanced sensitivity to the RAF inhibitor RAF709, which was confirmed in our model systems (44). However, whether this finding is generalizable to human lung cancers, which are notoriously heterogeneous, will require additional study. Another important question is whether similar effects will be seen with NRAS or HRAS-related cancers, where codon 61 mutations are more common.

It bears mentioning that the structure of the RAS multimer remains a topic of open debate. Multiple structural models have been proposed, with variable levels of experimental data (13-15,49). This likely reflects the low affinity of RAS-RAS interactions and that they rely on cell membrane association to occur. These characteristics lead to experimental challenges which have prevented rapid progress in solving structures. First, RAS-RAS interactions appear to be low affinity and dependent on association with the cell membrane making RAS complexes difficult to isolate. Second, RAS complexes may take multiple forms, making structural studies difficult

because most methods rely on obtaining a mono-dispersed population of structural conformers. As of now, the D154Q and R161E mutations are the only mutations we are aware of that appear to disrupt RAS multimers without altering other core biochemical functions of RAS. However, as new structural data becomes available, it may be possible to better delineate the conditions that dictate which structural forms occur and when and how to manipulate them.

If these findings can be validated in a larger set of human cancer specimens, they would have clinical significance, given the apparent difference in sensitivity of $KRAS^{Q61H}$-driven tumors to pharmacological MAPK inhibition. This idea is consistent with a trend towards clinical benefit in patients with codon 61 mutations in the SELECT-1 trial which tested the MEK inhibitor selumetinib in the context of KRAS-mutated lung cancer (50). It is worth noting that another KRAS mutation, $KRAS^{G12R}$ found in pancreatic cancer, also demonstrated a preference for MAPK signaling, prompting the initiation of a clinical trial of the MEK inhibitor selumetinib (NCT03040986). Together these studies highlight the possibility that trials of MAPK pathway inhibitors may turn positive if patient selection criteria is further refined to only include sensitive RAS mutations.

Acknowledgments

This work was supported by the V Foundation, DOD W81XWH-16-1-0106, CPRIT RP170373 (to KDW), startup fund for talented scholars of Daping Hospital and Research Institute, Third Military Medical University, Chongqing, China (to CX), the Giovanni Armenise–Harvard Foundation and the Lung Cancer Research Foundation (to CA), and Stand Up To Cancer-American Cancer Society Lung Cancer Dream Team Translational Research Grant (SU2C-AACR-DT17-15 to PAJ and CA). Stand Up To Cancer is a division of the Entertainment

Industry Foundation. Research grants are administered by the American Association for Cancer Research, the scientific partner of SU2C. Results shown in this report are derived from work performed at Argonne National Laboratory, Structural Biology Center at the Advanced Photon Source. Argonne is operated by U Chicago Argonne, LLC, for the U.S. Department of Energy, Office of Biological and Environmental Research under contract DE-AC02-06CH11357.

References

1. Prior IA, Lewis PD, Mattos C. A comprehensive survey of Ras mutations in cancer. Cancer Res **2012**;72:2457-67
2. Lito P, Solomon M, Li LS, Hansen R, Rosen N. Allele-specific inhibitors inactivate mutant KRAS G12C by a trapping mechanism. Science **2016**;351:604-8
3. Westover KD, Janne PA, Gray NS. Progress on Covalent Inhibition of KRAS(G12C). Cancer discovery **2016**;6:233-4
4. Janes MR, Zhang J, Li LS, Hansen R, Peters U, Guo X, *et al.* Targeting KRAS Mutant Cancers with a Covalent G12C-Specific Inhibitor. Cell **2018**;172:578-89 e17
5. Haigis KM. KRAS Alleles: The Devil Is in the Detail. Trends Cancer **2017**;3:686-97
6. Poulin EJ, Bera AK, Lu J, Lin Y-J, Strasser SD, Paulo JA, *et al.* Tissue-specific oncogenic activity of KRASA146T. Cancer discovery **2019**;9:738-55
7. Bera AK, Lu J, Wales TE, Gondi S, Gurbani D, Nelson A, *et al.* Structural basis of the atypical activation mechanism of KRAS(V14I). J Biol Chem **2019**;294:13964-72
8. Nan X, Tamguney TM, Collisson EA, Lin LJ, Pitt C, Galeas J, *et al.* Ras-GTP dimers activate the Mitogen-Activated Protein Kinase (MAPK) pathway. Proc Natl Acad Sci U S A **2015**;112:7996-8001
9. Plowman SJ, Ariotti N, Goodall A, Parton RG, Hancock JF. Electrostatic interactions positively regulate K-Ras nanocluster formation and function. Mol Cell Biol **2008**;28:4377-85
10. Spencer-Smith R, Koide A, Zhou Y, Eguchi RR, She F, Gajwani P, *et al.* Inhibition of RAS function through targeting an allosteric regulatory site. Nature chemical biology **2017**;13:62-8
11. Tian T, Harding A, Inder K, Plowman S, Parton RG, Hancock JF. Plasma membrane nanoswitches generate high-fidelity Ras signal transduction. Nature cell biology **2007**;9:905
12. Ambrogio C, Kohler J, Zhou ZW, Wang H, Paranal R, Li J, *et al.* KRAS Dimerization Impacts MEK Inhibitor Sensitivity and Oncogenic Activity of Mutant KRAS. Cell **2018**;172:857-68 e15
13. Lee KY, Fang Z, Enomoto M, Seabrook GG, Zheng L, Koide S, *et al.* Two Distinct Structures of Membrane-associated Homodimers of GTP- and GDP-bound KRAS4B Revealed by Paramagnetic Relaxation Enhancement. Angew Chem Int Ed Engl **2020**

14. Prakash P, Sayyed-Ahmad A, Cho KJ, Dolino DM, Chen W, Li H, *et al.* Computational and biochemical characterization of two partially overlapping interfaces and multiple weak-affinity K-Ras dimers. Sci Rep **2017**;7:40109
15. Muratcioglu S, Chavan TS, Freed BC, Jang H, Khavrutskii L, Freed RN, *et al.* GTP-Dependent K-Ras Dimerization. Structure **2015**;23:1325-35
16. Hunter JC, Manandhar A, Carrasco MA, Gurbani D, Gondi S, Westover KD. Biochemical and Structural Analysis of Common Cancer-Associated KRAS Mutations. Mol Cancer Res **2015**;13:1325-35
17. Drosten M, Dhawahir A, Sum EY, Urosevic J, Lechuga CG, Esteban LM, *et al.* Genetic analysis of Ras signalling pathways in cell proliferation, migration and survival. EMBO J **2010**;29:1091-104
18. Jafari R, Almqvist H, Axelsson H, Ignatushchenko M, Lundback T, Nordlund P, *et al.* The cellular thermal shift assay for evaluating drug target interactions in cells. Nat Protoc **2014**;9:2100-22
19. Xu CX, Jere D, Jin H, Chang SH, Chung YS, Shin JY, *et al.* Poly(ester amine)-mediated, aerosol-delivered Akt1 small interfering RNA suppresses lung tumorigenesis. American journal of respiratory and critical care medicine **2008**;178:60-73
20. Otwinowski Z, Minor W. Processing of X-ray diffraction data collected in oscillation mode. Methods Enzymol **1997**;276:307-26
21. Winn MD, Ballard CC, Cowtan KD, Dodson EJ, Emsley P, Evans PR, *et al.* Overview of the CCP4 suite and current developments. Acta Crystallogr D Biol Crystallogr **2011**;67:235-42
22. Emsley P, Lohkamp B, Scott WG, Cowtan K. Features and development of Coot. Acta Crystallogr D Biol Crystallogr **2010**;66:486-501
23. Adams PD, Afonine PV, Bunkoczi G, Chen VB, Davis IW, Echols N, *et al.* PHENIX: a comprehensive Python-based system for macromolecular structure solution. Acta Crystallogr D Biol Crystallogr **2010**;66:213-21
24. Williams CJ, Headd JJ, Moriarty NW, Prisant MG, Videau LL, Deis LN, *et al.* MolProbity: More and better reference data for improved all-atom structure validation. Protein Sci **2018**;27:293-315
25. Di Veroli GY, Fornari C, Wang D, Mollard S, Bramhall JL, Richards FM, *et al.* Combenefit: an interactive platform for the analysis and visualization of drug combinations. Bioinformatics **2016**;32:2866-8
26. Fritsch R, de Krijger I, Fritsch K, George R, Reason B, Kumar MS, *et al.* RAS and RHO families of GTPases directly regulate distinct phosphoinositide 3-kinase isoforms. Cell **2013**;153:1050-63
27. Ihle NT, Byers LA, Kim ES, Saintigny P, Lee JJ, Blumenschein GR, *et al.* Effect of KRAS oncogene substitutions on protein behavior: implications for signaling and clinical outcome. J Natl Cancer Inst **2012**;104:228-39
28. Zheng D, Wang R, Zhang Y, Pan Y, Cheng X, Cheng C, *et al.* The prevalence and prognostic significance of KRAS mutation subtypes in lung adenocarcinomas from Chinese populations. Onco Targets Ther **2016**;9:833-43
29. Gao B, Sun Y, Zhang J, Ren Y, Fang R, Han X, *et al.* Spectrum of LKB1, EGFR, and KRAS mutations in chinese lung adenocarcinomas. J Thorac Oncol **2010**;5:1130-5
30. Spoerner M, Hozsa C, Poetzl JA, Reiss K, Ganser P, Geyer M, *et al.* Conformational states of human rat sarcoma (Ras) protein complexed with its natural ligand GTP and their role for effector interaction and GTP hydrolysis. J Biol Chem **2010**;285:39768-78

31. Novelli E, First JT, Webb LJ. Quantitative Measurement of Intrinsic GTP Hydrolysis for Carcinogenic Glutamine 61 Mutants in H-Ras. Biochemistry **2018**
32. Harrison RA, Lu J, Carrasco M, Hunter J, Manandhar A, Gondi S, *et al.* Structural Dynamics in Ras and Related Proteins upon Nucleotide Switching. J Mol Biol **2016**;428:4723-35
33. Lu J, Bera AK, Gondi S, Westover KD. KRAS Switch Mutants D33E and A59G Crystallize in the State 1 Conformation. Biochemistry **2017**;57:324-33
34. Nassar N, Horn G, Herrmann CA, Scherer A, McCormick F, Wittinghofer A. The 2.2 Å crystal structure of the Ras-binding domain of the serine/threonine kinase c-Raf1 in complex with RaplA and a GTP analogue. Nature **1995**;375:554-60
35. Lavoie H, Therrien M. Regulation of RAF protein kinases in ERK signalling. Nat Rev Mol Cell Biol **2015**;16:281-98
36. Freeman AK, Ritt DA, Morrison DK. Effects of Raf dimerization and its inhibition on normal and disease-associated Raf signaling. Mol Cell **2013**;49:751-8
37. Jin T, Lavoie H, Sahmi M, David M, Hilt C, Hammell A, *et al.* RAF inhibitors promote RAS-RAF interaction by allosterically disrupting RAF autoinhibition. Nature communications **2017**;8:1211
38. Pacold ME, Suire S, Perisic O, Lara-Gonzalez S, Davis CT, Walker EH, *et al.* Crystal structure and functional analysis of Ras binding to its effector phosphoinositide 3-kinase gamma. Cell **2000**;103:931-43
39. Terrell EM, Durrant DE, Ritt DA, Sealover NE, Sheffels E, Spencer-Smith R, *et al.* Distinct Binding Preferences between Ras and Raf Family Members and the Impact on Oncogenic Ras Signaling. Mol Cell **2019**;76:872-84 e5
40. Fabian JR, Vojtek AB, Cooper JA, Morrison DK. A single amino acid change in Raf-1 inhibits Ras binding and alters Raf-1 function. Proc Natl Acad Sci U S A **1994**;91:5982-6
41. Rajakulendran T, Sahmi M, Lefrancois M, Sicheri F, Therrien M. A dimerization-dependent mechanism drives RAF catalytic activation. Nature **2009**;461:542-5
42. Yao Z, Yaeger R, Rodrik-Outmezguine VS, Tao A, Torres NM, Chang MT, *et al.* Tumours with class 3 BRAF mutants are sensitive to the inhibition of activated RAS. Nature **2017**;548:234-8
43. Lavoie H, Thevakumaran N, Gavory G, Li JJ, Padeganeh A, Guiral S, *et al.* Inhibitors that stabilize a closed RAF kinase domain conformation induce dimerization. Nature chemical biology **2013**;9:428
44. Shao W, Mishina YM, Feng Y, Caponigro G, Cooke VG, Rivera S, *et al.* Antitumor Properties of RAF709, a Highly Selective and Potent Inhibitor of RAF Kinase Dimers, in Tumors Driven by Mutant RAS or BRAF. Cancer Res **2018**;78:1537-48
45. Marani M, Hancock D, Lopes R, Tenev T, Downward J, Lemoine NR. Role of Bim in the survival pathway induced by Raf in epithelial cells. Oncogene **2004**;23:2431-41
46. Ianevski A, He L, Aittokallio T, Tang J. SynergyFinder: a web application for analyzing drug combination dose-response matrix data. Bioinformatics **2017**;33:2413-5
47. Gupta S, Ramjaun AR, Haiko P, Wang Y, Warne PH, Nicke B, *et al.* Binding of ras to phosphoinositide 3-kinase p110α is required for ras-driven tumorigenesis in mice. Cell **2007**;129:957-68
48. Cagnol S, Chambard JC. ERK and cell death: Mechanisms of ERK-induced cell death–apoptosis, autophagy and senescence. The FEBS journal **2010**;277:2-21
49. Jares-Erijman EA, Jovin TM. FRET imaging. Nat Biotechnol **2003**;21:1387-95

50. Jänne PA, van den Heuvel MM, Barlesi F, Cobo M, Mazieres J, Crinò L, *et al.* Selumetinib Plus Docetaxel Compared With Docetaxel Alone and Progression-Free Survival in Patients With KRAS-Mutant Advanced Non–Small Cell Lung Cancer: The SELECT-1 Randomized Clinical Trial. Jama **2017**;317:1844-53

Figure legends

Fig. 1. **KRAS^{Q61H} interacts preferentially with RAF-RBD over p110α/γ-RBD**. (**A**) A schematic model for preferential interactions between KRAS G12D or Q61H and downstream effectors RAF or p110. (**B**) Immunoprecipitation of CFP-tagged RAS mutants using c-RAF or p110γ RBDs. HEK293T cells were harvested after 48 hrs transfection with CFP-tagged KRAS mutants in the presence of 10% FBS. The protein samples were subject to pull-down and Western blotting assay. IP, immunoprecipitation; WT, wild type; exp, exposure. (**C**) Quantitation of Fig. 1B demonstrates enhanced interactions between c-RAF-RBD and KRAS^{Q61H} relative to KRAS^{G12D} but not with p110γ-RBD (n = 3). (**D**, **E**) KRAS^{Q61H} enhances the thermal stability of c-RAF expressed in HEK293T cells relative to other RAS mutations. However, KRAS^{G12D} enhances the thermal stability of PI3K subunit p110α relative to other RAS mutations. Bars represent quantitation of blots above. HEK293T cells were harvested after 48 hrs co-transfection of KRAS mutants with c-RAF or p110α in the presence of 10% FBS. The protein samples were subject to thermal exposure and the resultant supernatants were subject to Western blotting assay for testing the remaining level of c-RAF, p110α, or RAS (n = 3). WT, wild type. For all bar graphs, data are presented as mean ± SD. * $p<0.05$, ** $p<0.01$, and *** $p<0.001$ compared to KRAS^{G12D} (Two-way ANOVA).

Fig. 2. **NSCLC patient specimens show differential AKT and ERK signal output for KRAS^{G12D} and KRAS^{Q61H}**. (**A**) Screening results of NSCLC patient specimens for KRAS mutations. In total, there were 1,006 NSCLC patient tumor samples selected for *KRAS*, *EGFR*, *PI3K*, *ALK*, and *BRAF* sequencing and three samples were KRAS^{Q61H} mutant. (**B**) Immunohistochemical staining for p-AKT and p-ERK in patient specimens demonstrate

increased p-ERK in $KRAS^{Q61H}$ patients relative to $KRAS^{G12D}$ and increased p-AKT in $KRAS^{G12D}$ patients relative to $KRAS^{Q61H}$ (scale bar: 100 μm). WT, wild type. (**C**) H-scores of p-AKT and p-ERK levels from IHC staining samples (n = 15). WT, wild type. (**D**, **E**) Representative blots and associated quantitation from frozen tissue specimens for p-AKT and p-ERK in NSCLC patient specimens (n = 3). WT, wild type; ns, no significance. For all graphs, data are presented as the mean ± SD.

Fig. 3. **Crystal structure of $KRAS^{Q61H}$:GTP**. (**A**-**F**) Comparison of X-ray crystal structures of $KRAS^{Q61H}$ and $KRAS^{G12D}$ demonstrating alterations in switch 2 (green) conformation. Switch 1 is in yellow and GTP in sticks. Difference Fourier F_o-F_c electron density map of GTP at 3σ contour level is shown in green in **B**. (**G**) Superimposition of the 6 molecules in the asymmetric crystallographic unit reveals an ensemble of backbone and His61 conformations in $KRAS^{Q61H}$. (**H**) Structure comparison of $HRAS^{G12C}$:GMPPNP (4L9W) in light magenta, $KRAS^{Q61H}$:GMPPNP (3GFT) in dark salmon, $HRAS^{G12D}$:GMPPNP (1AGP) in pale yellow, $KRAS^{G12D}$:GMPPNP (5USJ) in slate, Mg^{2+} in sphere (magenta), GTP and Gln61 are in sticks. (**I**) Distances between side chain nitrogen of residue 61 and γ phosphate of GTP are shown in red and blue respectively for $KRAS^{Q61H}$ and $KRAS^{G12D}$. (**J**) Distance between the side chain nitrogen of residue 61 (Q or H) and γ-phosphate of GTP over the time course of 50 ns simulation.

Fig. 4. **RAF and $KRAS^{Q61H}$ multimerization are cooperative.** (**A**) Immunoprecipitation of active form of CFP-tagged KRAS WT, G12D, G13D, and Q61H and the counterparts with D154Q mutants, using c-RAF or p110γ RBDs. D154Q is added to prevent RAS multimerization.

HEK293T cells were harvested after 48 hrs transfection with CFP-tagged KRAS mutants in the presence of 10% FBS. The protein samples were subject to pull-down and Western blotting assay. IP, immunoprecipitation; WT, wild type. (**B**, **C**) Quantitation of Fig. 4A demonstrates that $KRAS^{Q61H}$ multimerization influences interactions with c-RAF but not p110γ. Data were normalized to $KRAS^{G12D}$ and the RAS-GTP level for KRAS mutants was compared in the presence or absence of D154Q mutation (n = 3). IP, immunoprecipitation; WT, wild type. (**D**) CFP emission after photobleaching indicates multimerization between CFP and YFP-fused KRAS. All KRAS mutants except for Q61H retain the ability to dimerize regardless of expression of exogenous c-RAF, including the dimer-incompetent form R89L. HEK293T cells were co-transfected with c-RAF, CFP-KRAS, and YFP-KRAS constructs and subject to confocal microscopy for FRET assay. WT, wild type. (**E**) Schematic of RAS-RAF cooperativity. Left, a cooperative RAS-RAF heterotetramer including autoregulatory CRD and RBD domains of endogenous c-RAF (blue). Middle, introduction of exogenous $c\text{-}RAF^{R89L}$ (green) impairs $KRAS^{Q61H}$ multimerization by heterodimerizing with endogenous c-RAF. However, introduction of exogenous $c\text{-}RAF^{R89L/R401H}$ which is unable to dimerize with endogenous c-RAF, allows recovery of KRAS dimers (right). WT, wild type; CRD, cysteine-rich domain; RBD, Ras-binding domain; KD, kinase domain. (**F**) CFP emission after photobleaching indicates multimerization between CFP- and YFP-fused $KRAS^{G12D}$ and $KRAS^{Q61H}$. Introduction of R401H into $c\text{-}RAF^{R89L}$ restored FRET signal for $KRAS^{Q61H}$. The FRET assays were performed in HEK293T cells co-transfected with c-RAF, CFP-KRAS, and YFP-KRAS constructs via confocal microscopy. (**G**) FRET from multimerization of fluorescent-tagged c-RAF is not observed by the dimer-disrupting mutation D154Q in KRAS. HEK293T cells were co-transfected with c-RAF-CFP, c-RAF-YFP, and KRAS constructs and subject to confocal

microscopy for FRET assay. All FRET data are presented as the mean ± SEM. WT, wild type. (**H**) Signal transduction in HEK293T cells demonstrates a preference for MAPK signaling for $KRAS^{Q61H}$ relative to $KRAS^{G12D}$ and $KRAS^{G13D}$. HEK293T cells were harvested after 48 hrs co-transfection of KRAS mutants in the presence of 10% FBS. The protein samples were subject to Western blotting assay for testing RAS signals. WT, wild type. (**I**) Quantitative comparison of the "dimer dependency" ratio consisting of the ratio between normalized MAPK signal (p-ERK/t-ERK) or PI3K (p-AKT/t-AKT) for dimer-competent vs. dimer-impaired (D154Q) KRAS. This demonstrates a difference in dimer-dependent signaling for MAPK, but not PI3K for $KRAS^{G13D}$ and $KRAS^{Q61H}$. WT, wild type. For all graphs related to blots, data are presented as the mean ± SD. *p<0.05 and ***p<0.001 (Two-way ANOVA).

Fig. 5. **Differential responses upon the exposure to MEK and RAF inhibitors *in vitro* and *in vivo***. (**A**, **B**, **C**) IC_{50} values in response to MEK and RAF inhibitors treatment of $KRas^{lox}$ $KRAS^{MUT}$ MEFs expressing exogenous HA-tagged $KRAS^{G12D}$ or $KRAS^{Q61H}$ demonstrate higher sensitivity for Q61H relative to G12D. Data are presented as mean ± SD of cell lines belonging to each group. IC_{50} values were 1,140 nM vs. 224 nM for selumetinib, 10 nM vs 2 nM for trametinib, 4,300 nM vs. 300 nM for RAF709 for G12D and Q61H, respectively. (**D**) Cell growth curve of $KRas^{lox}$ $KRAS^{MUT}$ MEFs expressing exogenous HA-tagged $KRAS^{G12D}$ or $KRAS^{Q61H}$ in the absence of endogenous wild-type *KRas* alleles upon exposure to Sel (100 nM), Tra (10 nM), or RAF709 (1 μM) alone or in combination. Results were assessed by IncuCyte measurements and are representative of one of three similar experiments. Sel, selumetinib; Tra, trametinib. (**E**, **F**) Differential synergistic effects of RAF inhibitor in combination with MEK inhibitor. Heatmap of Bliss score for $KRas^{lox}$ $KRAS^{MUT}$ MEFs expressing exogenous HA-tagged

$KRAS^{G12D}$ or $KRAS^{Q61H}$ upon the exposure to RAF709 in combination with trametinib. Positive score indicates combinations where the effect is greater than additive. (**G**) Fold volume change in mouse tumor implants derived from of *KRas*^{lox} $KRAS^{MUT}$ MEFs expressing exogenous HA-tagged $KRAS^{G12D}$ or $KRAS^{Q61H}$ when treated with Sel (50 mg/kg daily). Sel, selumatinib.

Figure 1

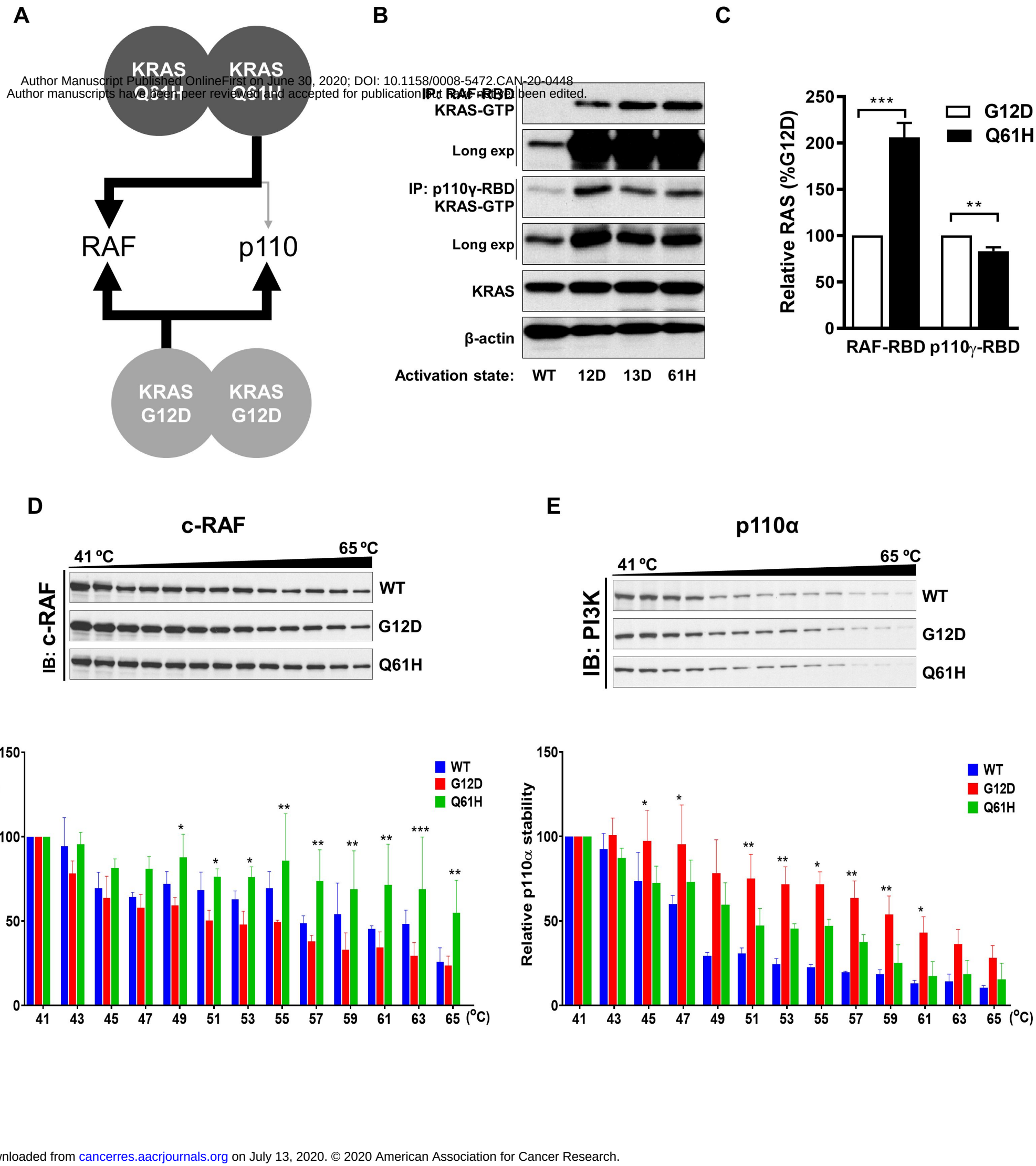

Figure 2

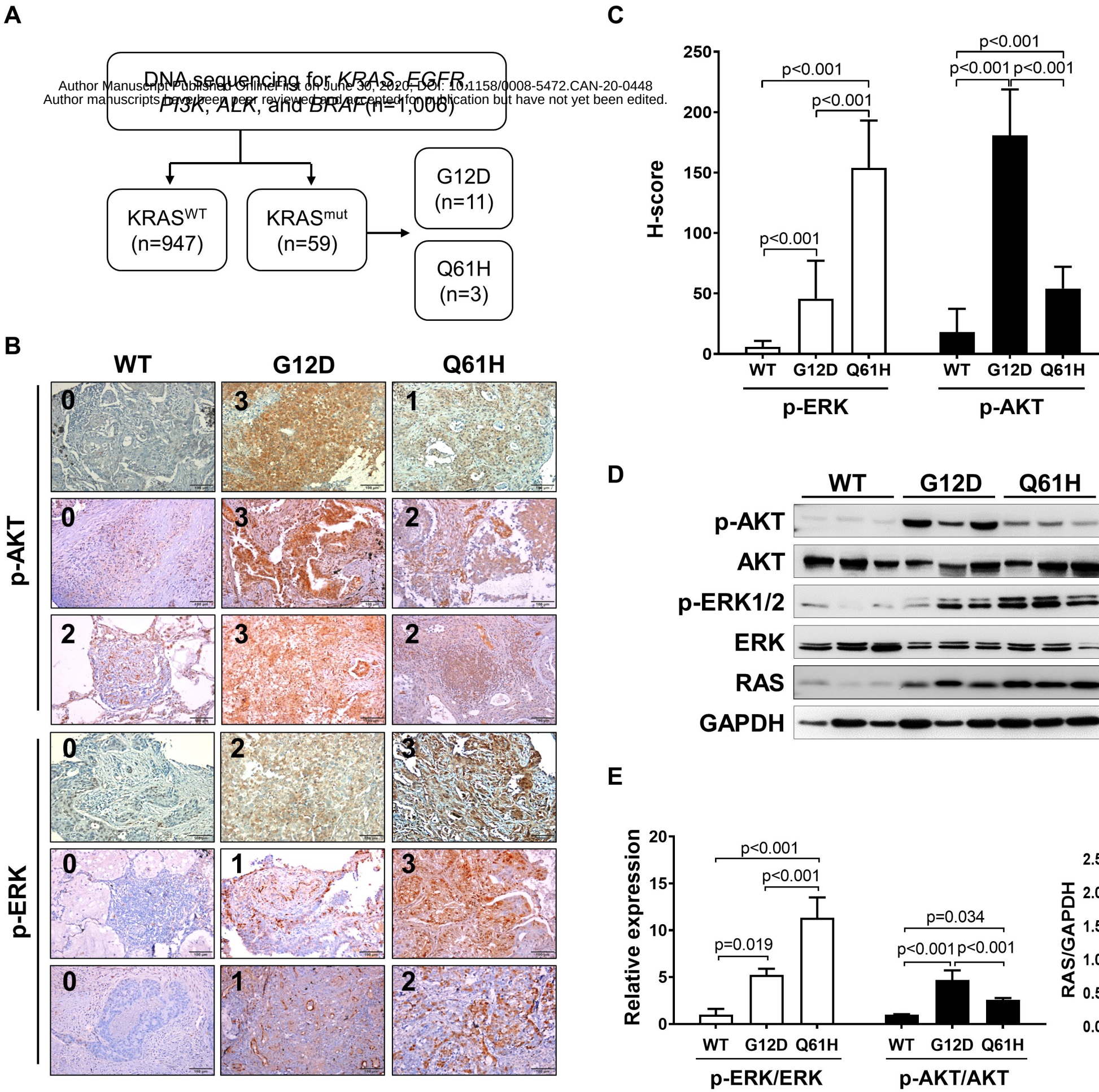

Figure 3

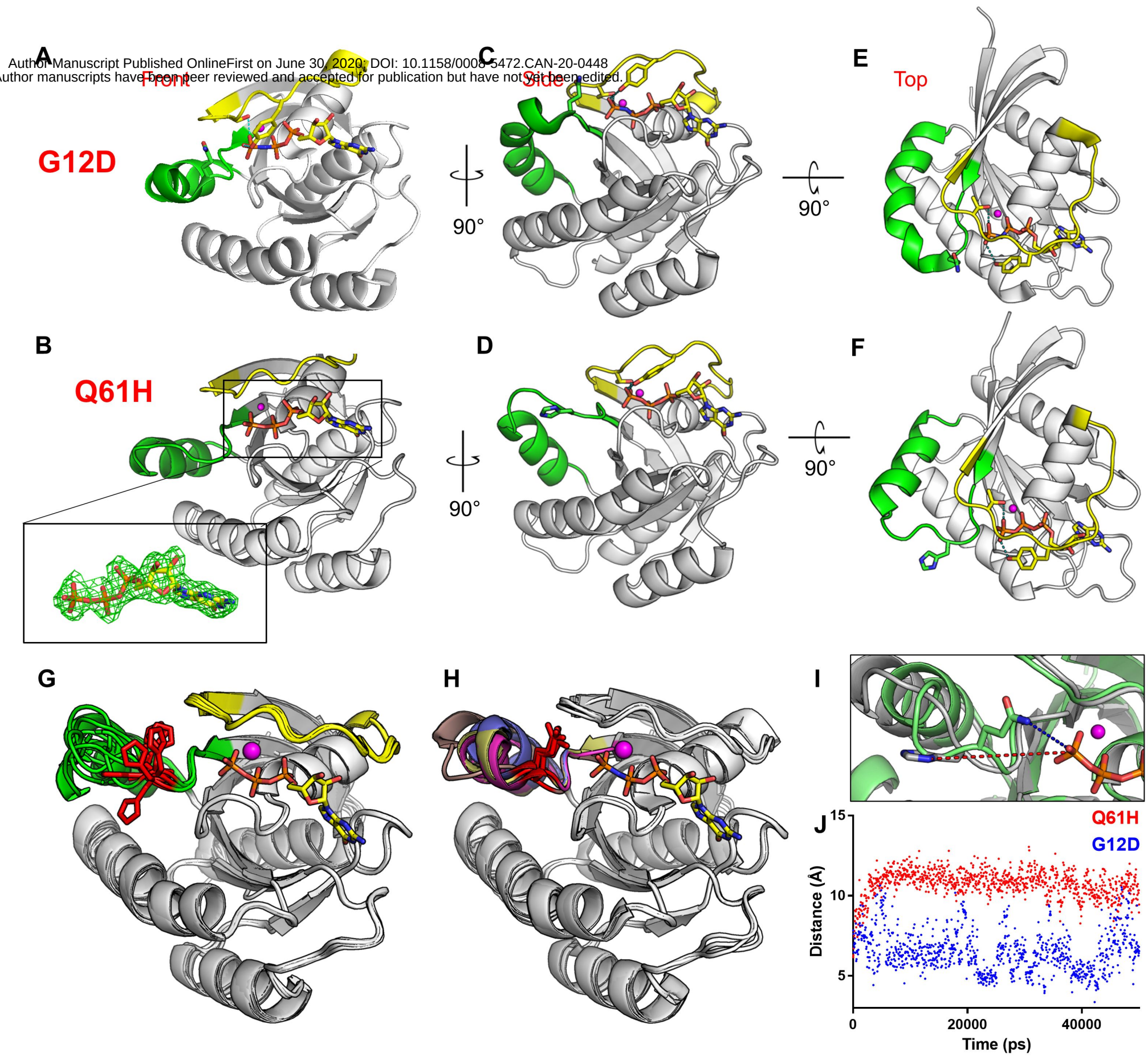

Figure 4

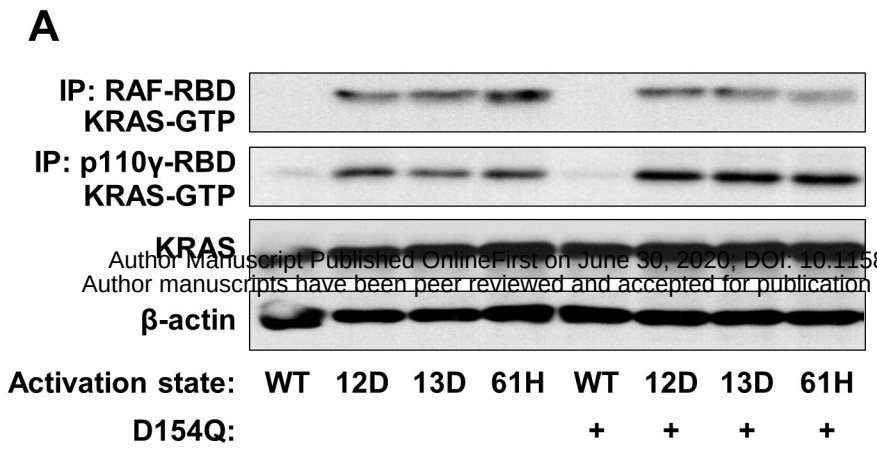

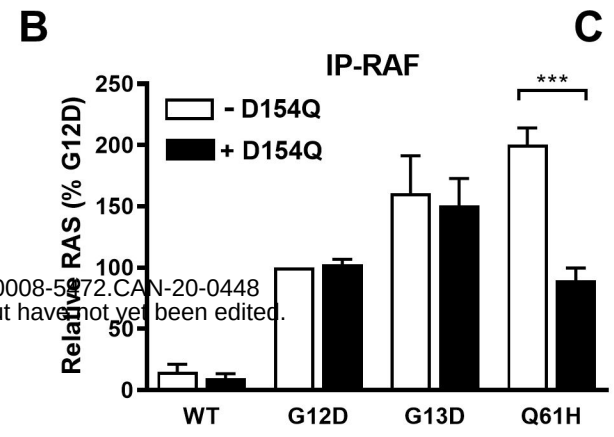

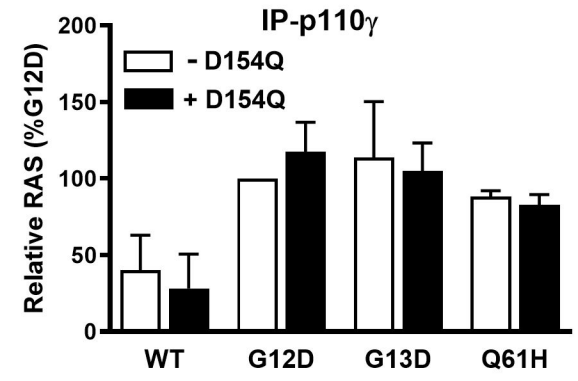

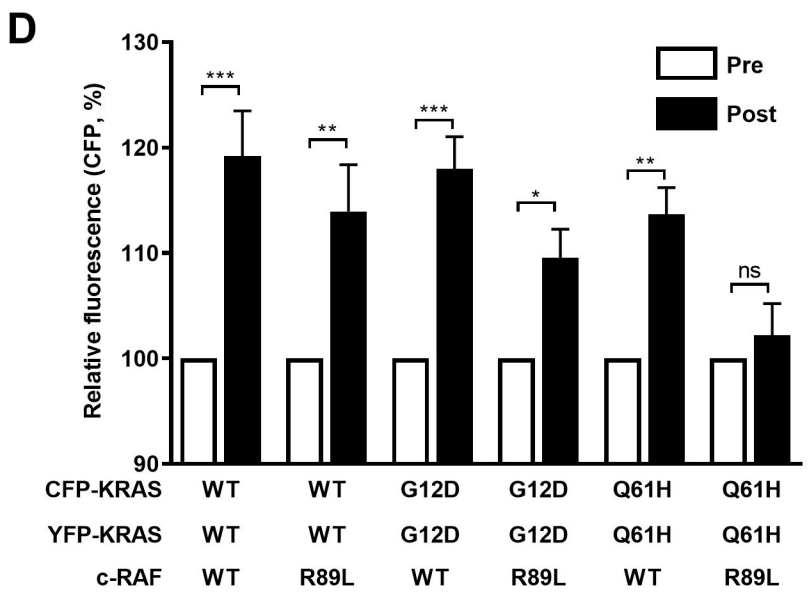

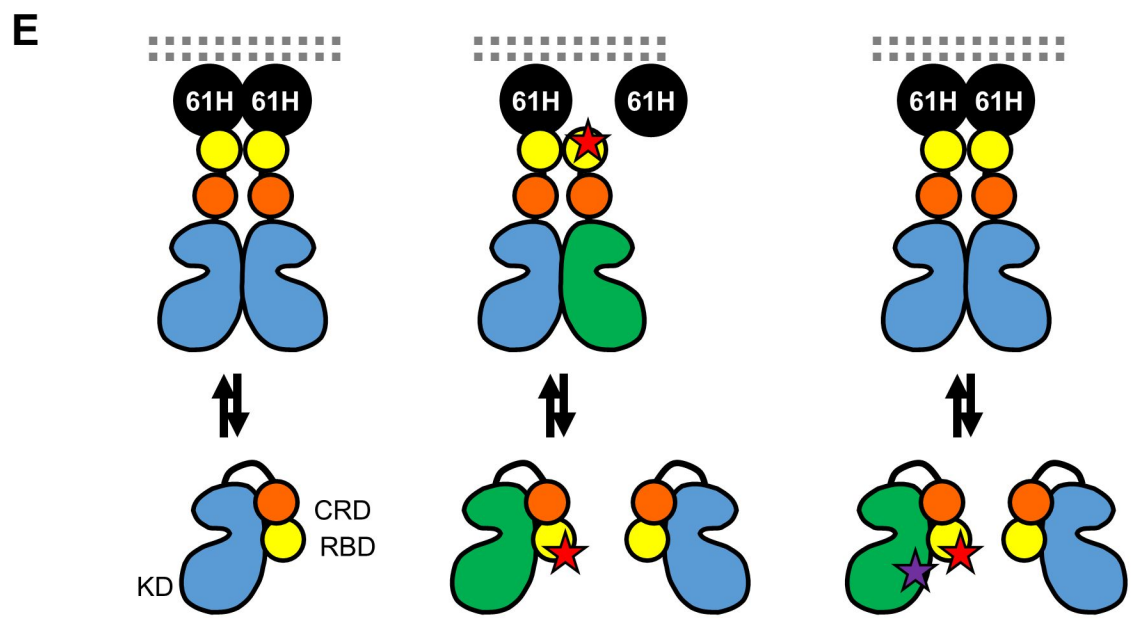

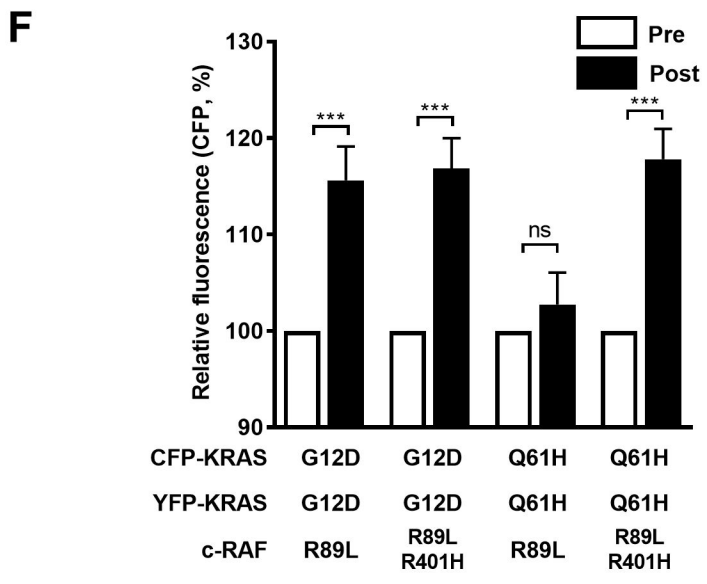

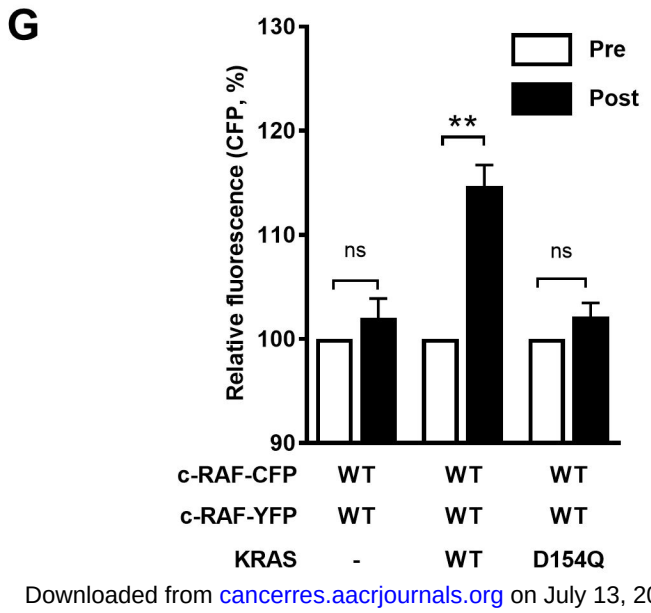

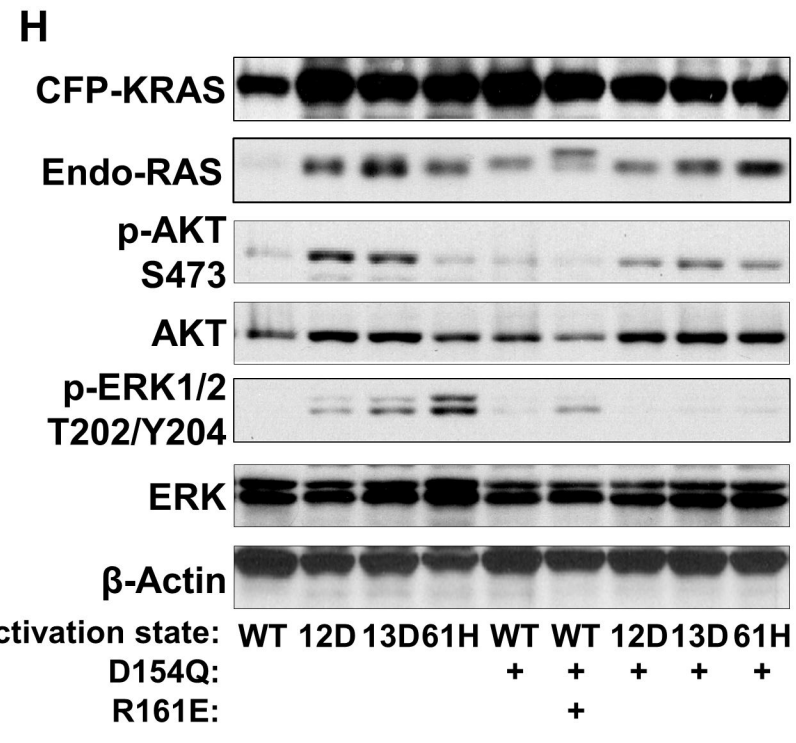

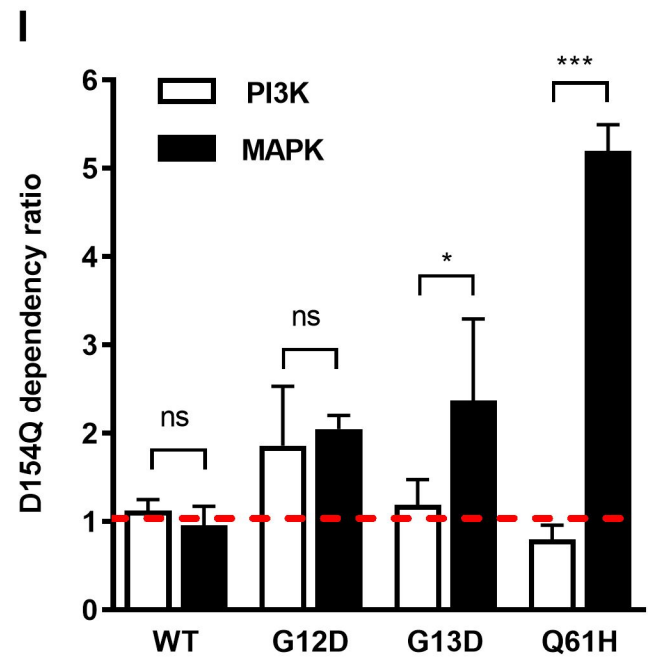

Figure 5

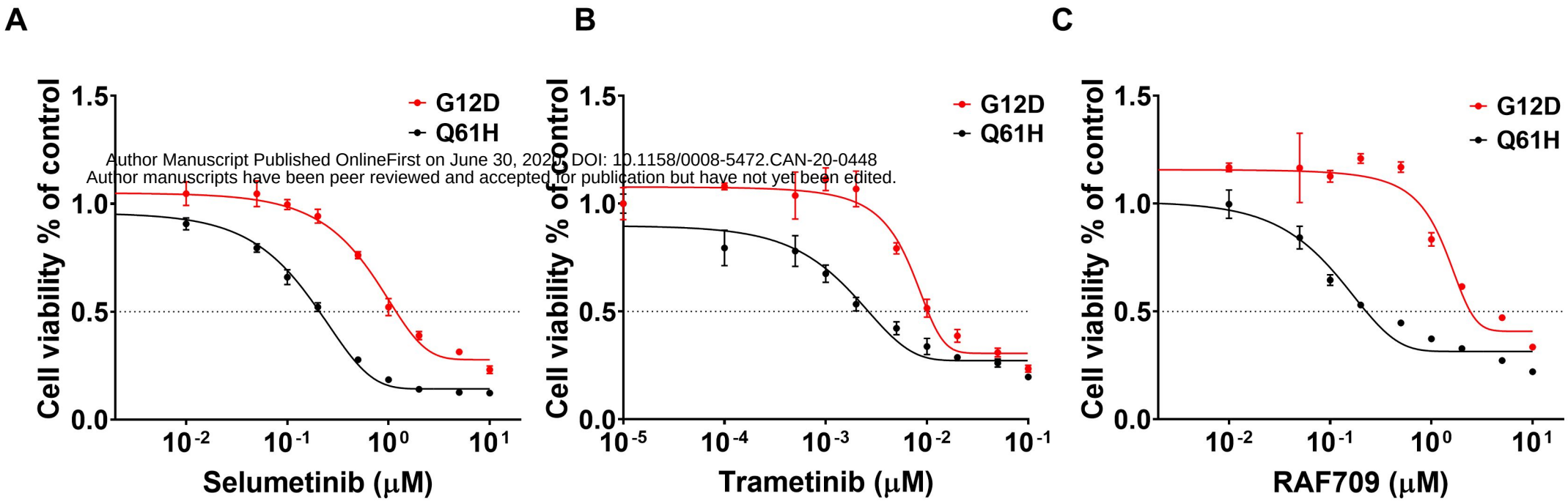

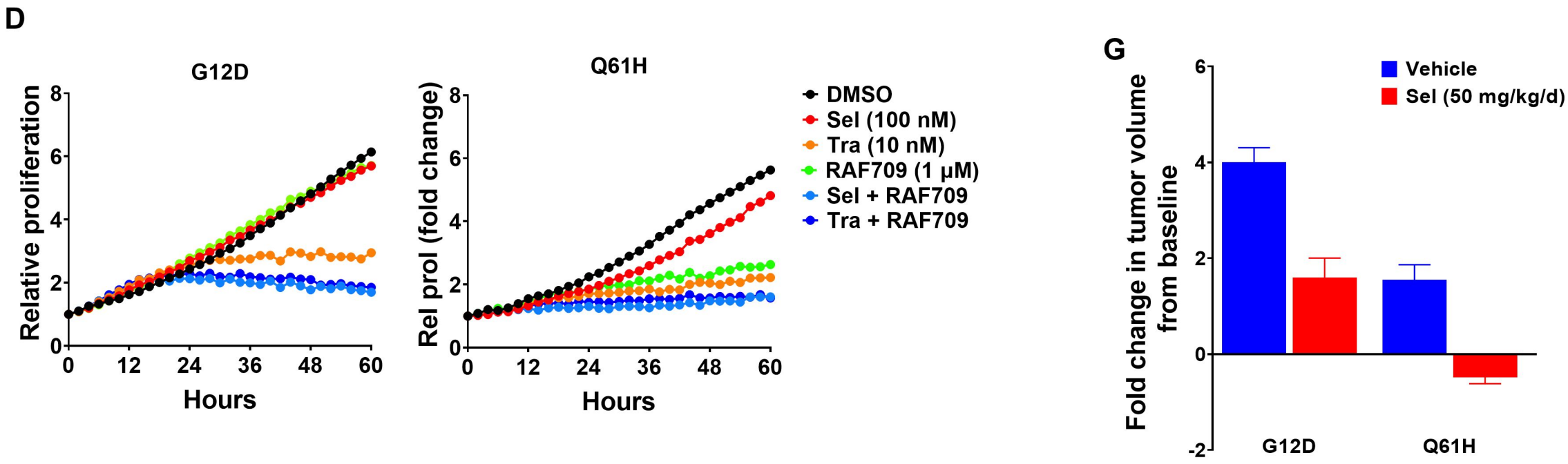

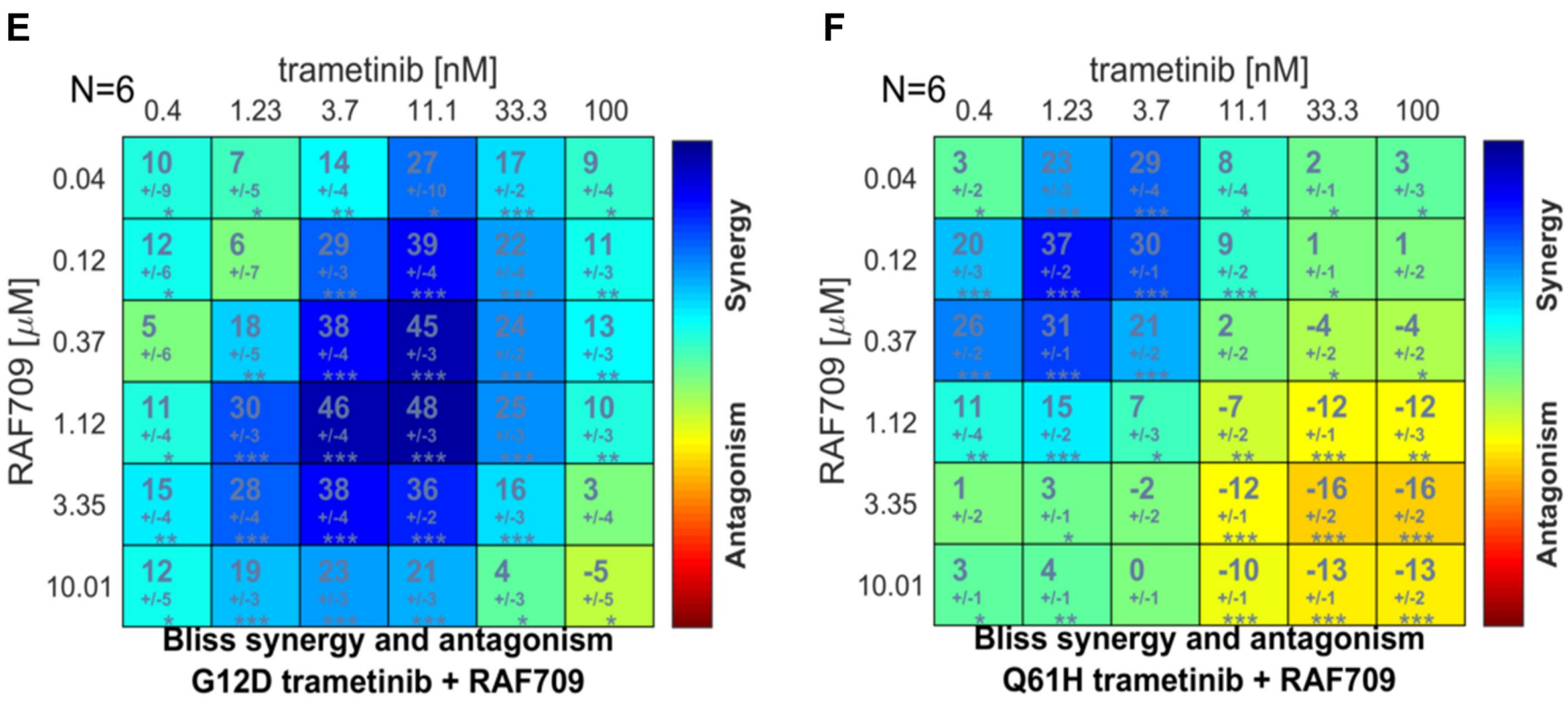

Cancer Research
The Journal of Cancer Research (1916–1930) | The American Journal of Cancer (1931–1940)

AACR American Association for Cancer Research

KRASQ61H preferentially signals through MAPK in a RAF dimer-dependent manner in non-small cell lung cancer

Zhi-Wei Zhou, Chiara Ambrogio, Asim K Bera, et al.

Cancer Res Published OnlineFirst June 30, 2020.